Development and Evaluation of a Smart Platform for Engineered Electroceutical

Dressings (SPEEDs)

Thesis

Presented in Partial Fulfillment of the Requirements for the Degree Master of Science in

the Graduate School of The Ohio State University

By

Rachel Mary Heald

Graduate Program in Mechanical Engineering

The Ohio State University

2021

Thesis Committee

Dr. Shaurya Prakash, Advisor

Dr. Traci Wilgus, Committee Member

Abstract

Nearly 6.5 million human patients battle with chronic wounds in the United States, costing an estimated $6.5 billion each year. In addition to this, domestic and livestock animal chronic wound management is predicted to cost an additional $1.1 billion. In addition to the economic impact, chronic wounds present technological and clinical challenges of evaluating wound healing and infection mitigation. Previously, the printed electroceutical dressing (PED) has been reported to eradicate biofilms *in vitro*. However, the PED only partially addresses the challenges with chronic wound healing. Therefore, a smart platform for engineered electroceutical dressings (SPEEDs) that can control treatment dosing, integrate sensors, and exist as a flexible system is presented. In this thesis, efforts to develop the previous PED into SPEEDs is focused on treatment dosing control, a flexible power source, and a Bluetooth® integrated circuit while continuing to evaluate the electroceutical to heal chronic wounds.

In vivo, the PED was utilized as an intervention treatment to heal chronic wounds in a dog and a cat. Both animals underwent standard, established wound care for >1 year (dog) and 8 months (cat). The PED eliminated infection in the dog and the cat after 10 and 17 days of treatment, respectively. Full healing of the dog chronic wound was observed after 67 days and the cat chronic wound was fully healed after 47 days. This proven efficacy to heal chronic wounds with infection *in vivo* motivated the development of a murine wound model to evaluate the PED's ability to heal uninfected wounds. Two pilot mice studies were conducted and determined pitfalls in the current design of the PED. Mainly,

the rigidity of the battery and circuit connections. Thereby, motivating the development of a flexible battery for SPEEDs.

A conformable, silver-zinc battery wetted by wound fluid to act as the electrolyte has been fabricated for preliminary integration with SPEEDs. The Ag/AgCl-Zn cells placed in series scale nearly linear in voltage, producing voltages comparable to the 6 V commercial battery pack in use when 9 cells are connected in series (6.27 V). In addition to full conformability of SPEEDs, a preliminary three-electrode design for controlled dosing is presented. A preliminary Bluetooth® enabled circuit was also integrated with SPEEDs *in vitro* for remote monitoring of the current flow within the wound bed.

Vita

2015 – Seaman High School, Topeka, KS

2019 – Bachelor of Science with Bioengineering Certificate, Mechanical Engineering,

University of Kansas, Lawrence, KS

2020 to present – Graduate Research Assistant, Department of Mechanical and

Aerospace Engineering, The Ohio State University, Columbus, OH

Publications

- Heald R, Bennett M, Subramaniam VV, Dusane D, Lochab V, Mohana Sundaram P, Salyer S, West JD, Stoodley P, Prakash S. Printed electroceutical dressings for the inhibition of biofilms and treatment of chronic wounds. *JMEMS*. 2020;29(5):918-923.

- *In Review:* Heald R, Salyer S, Ham K, Wilgus T, Subramaniam VV, Prakash S. Electroceutical treatment of infected chronic wounds in a dog and a cat. *Vet Surg.*

Fields of Study

Major Field: Mechanical Engineering

Table of Contents

List of Tables

List of Figures

Chapter 1. Introduction

1.1 Motivation

Chronic wounds are defined as wounds that fail to heal in 4-6 weeks (1, 2). Often, chronic wounds show significant presence of bacterial infection (3–5) with recalcitrance towards standard antimicrobial treatment (6, 7). Therefore, chronic wound management and treatment presents a major healthcare and financial burden on the United States with nearly 6.5 million human patients costing an estimated $6.5 billion annually (8). Moreover, domestic and livestock animal chronic wound management is predicted to cost an additional $1.1 billion by 2021 with an expected increase of 7% per year (9). In addition to the economic impact, chronic wounds present technological and clinical challenges of evaluating wound healing and infection mitigation, which is currently conducted by clinical, visual observation and by punch biopsies for infection. Our group has previously reported a novel, conformable printed electroceutical dressing (PED) for the eradication of biofilms *in vitro* (10, 11). However, the PED is limited in its ability to provide precise treatment dosing and lacks the technology to evaluate clinically relevant metrics of wound healing or infection. Therefore, work towards an electroceutical dressing that can precisely control dosing, integrate clinically relevant sensors, and exist as a fully flexible system permitting contouring to different anatomically located wounds, referred to as a smart platform for engineered electroceutical dressings (SPEEDs), is presented in this thesis.

1.2 Specific Aims of this Research

The specific aims of this Master's Thesis project are:

1. Introducing treatment methodology for the application of the PED used *in vivo* as an intervention treatment for veterinary chronic wounds.

2. Formulating a scientifically significant study to evaluate PED treatment in uninfected wounds.

3. Developing SPEEDs with a fully flexible, Bluetooth® enabled device with control of treatment dosing.

1.3 Background

In addition to an economic burden, chronic wounds pose significant scientific, technological, and clinical challenges (12). Nearly 78% of human chronic wound infections contain complex communities of bacteria called biofilms (13–17). The bacteria in biofilms have lower metabolic needs than planktonic bacteria (non-adherent cells considered to be free-living as opposed to those bacterial communities encapsulated in extracellular polymeric substances that form biofilms (18)) and are encapsulated within a three-dimensional (3D) structure of extracellular polymeric substances (EPS) (19). Such characteristics allow the bacteria to exhibit avoidant or resistant behavior to state-of-art treatments with antimicrobials and host immune defenses (20). While the presence of bacterial biofilms has been attributed to delayed healing for chronic wounds in humans, the role of biofilm infection in veterinary patients is ill-defined (21–25). Moreover, in both

veterinary and human patients, molecular diagnostic methods have identified a broad spectrum of microorganisms suggesting that chronic wound infections are often polymicrobial (26–30). Additionally, it has been found that bacteria forming into biofilms possess mechanisms to encourage a diverse set of bacteria to form a polymicrobial biofilm (31). Polymicrobial infections and biofilms often increase the severity and recalcitrance of the infection due to the amount and diversity of bacteria present (31).

Current clinical practice for bacterial clearance of chronic wounds uses mechanical debridement or a combination of debridement with existing antimicrobials (4, 32–37). Mechanical debridement is considered the 'gold standard' to remove necrotic tissue and microorganisms to obtain a clean wound bed (38). However, bacteria remaining in the wound may resist the debridement process and serve as a treatment-resistant reservoir of bacterial cells that leads to delays in healing (39). Debridement paired with skin grafts and negative pressure dressings have shown to be successful in some cases (39), but using multiple or combinatorial treatments can be both costly and prolongs treatment over extended time periods. Moreover, for chronic infections, debridement has been noted to be only modestly effective (40–43). Negative pressure dressings have shown some efficacy by altering the biofilm architecture by reducing the overall thickness and biomass, but bacterial cell viability does not change (44). Clearly, the current state of art treatment options for infected chronic wounds relies on a multi-faceted approach with limited success.

Bioactive dressings have emerged to stimulate wound healing in chronic wounds (Table 1). MiMedx Epifix®, a dehydrated anion membrane allograft, is a dressing formed

from the amniotic membrane of a human placenta, where the extracellular matrix (ECM) is continually remodeled within the tissue (45). Chitosan-based dressings are used for the antimicrobial properties of chitosan, a natural polymer. There are many commercialized chitosan products for wound healing such as gels, sponges, gauzes, and patches that are biodegradable (46). Collagen dressings (DermaRite) address the elevated levels of matrix metalloproteinases (MMPs) that are known to be a key component of chronic wounds by degrading both non-viable and viable collagen within the wound (47). The strategy to heal chronic wounds by bioactive dressings rely on the delivery of bioactive molecules to promote wound healing rather than eliminating infection (48). Some bioactive dressings may exhibit antimicrobial properties but have not demonstrated efficacy against bacterial biofilms (46, 48, 49).

Table 1. Summary of bioactive wound dressings used to stimulate wound healing and heal chronic wounds.

Dressing	Advantages
MiMedx Epifix® (dehydrated amnion/chorion membrane allograft)	- Protective barrier - Provides a human biocompatible extracellular matrix (ECM) - Retains 300+ regulatory proteins
Chitosan-based Dressings	- Antimicrobial biopolymer - Many commercialized forms: films, sponges, gauze, gels, patches - Biodegradable
DermaRite Collagen Dressings	- Addresses elevated levels of matric metalloproteinases (MMPs) - Maintains moist wound environment

Recently, it was reported that bacteria rely on electrostatic interactions for adhesion to surfaces (50), thereby motivating the evaluation of electrical stimulation as a possible bacterial inhibitory agent. Electric fields were first suggested to have possible inhibitory

effects against biofilms in 1992 (51). On other hand, the presence of endogenous electric

fields for wound healing has been considered since the work of DuBois and identification

of the 'skin battery' in the 1850s (52–55). The transepithelial electric potential (TEP) that

is the 'skin battery' ranges from 10 mV to 60 mV, depending on the location (53). When

the skin is wounded and the epithelial barrier is broken, the TEP short-circuits and causes

a potential drop at the wound location (Figure 1). This potential gradient allows current to

flow towards the wound, creating electric fields (56). The current density within skin

wounds have been measured to be 4-8 $\mu A/cm^2$ with electric fields at 40-150 V/m (57, 58).
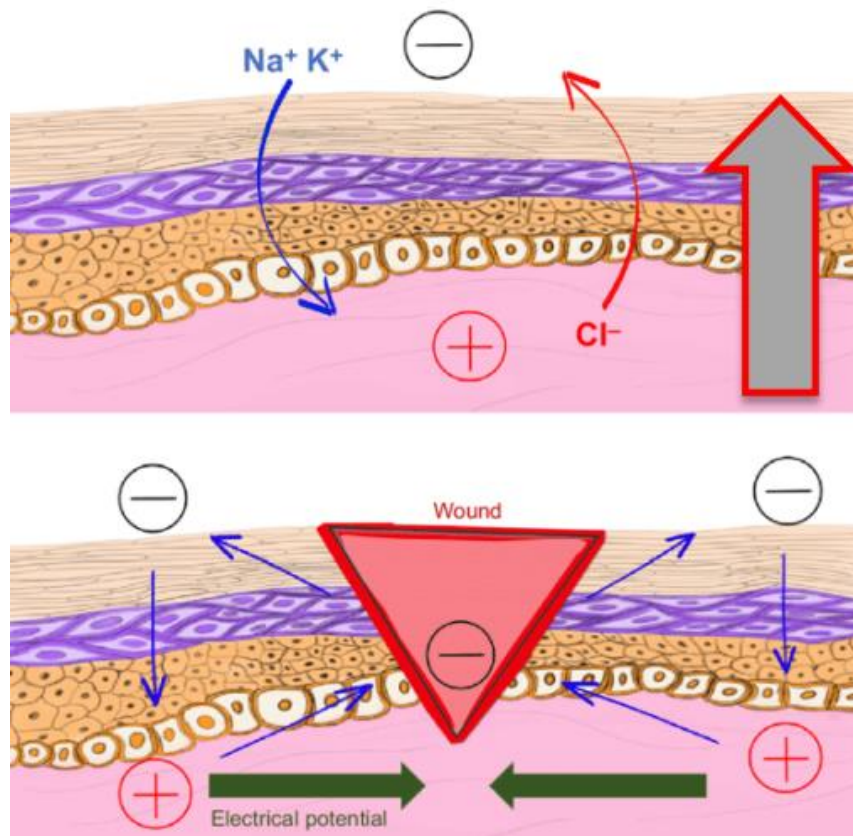
Figure 1. (top) The depiction of the 'skin battery' with the transepithelial potential created due to the ionic movement of Na+, K+, and Cl-. (bottom) The wounded skin 'short circuits' the 'skin battery' and creates an electric potential gradient with current flowing out of the wound. Figure from Hunckler et al. 2017.

The presence of the potential gradient within broken epidermis is one of many factors that can influence cell migration upon wounding (54). Table 2 shows a summary of the influence of electrical stimulation on key host cells. Keratinocytes have shown to migrate in an electric field as low as 25 V/m directionally towards the cathode, the same direction as endogenous electric fields in wounds (59). Additionally, electric fields of 100 V/m have demonstrated keratinocyte proliferation (60). Both fibroblasts and macrophages have been shown to migrate towards the anode in electric fields of physiological strength (50-300 V/m) (61, 62). Neutrophils, similar to keratinocytes, migrate towards the cathode in fields of 50-100 V/m (57). Moreover, electrical stimulation has shown to promote angiogenesis and reduce wound dimensions in comparison to traditional wound care (63).

Table 2. Summary of host cells in response to electrical stimulation.

Cell	Electrical Stimulation Response
Keratinocytes (59, 60)	- Migrate towards cathode (25-100 V/m) - Increased proliferation (100 V/m)
Fibroblasts (62)	- 164 gene transcripts increased; 302 gene transcripts decreased (100 V/m) - Migrate towards anode (50-100 V/m)
Endothelial Cells (63)	- Increased vascular endothelial growth factor (VEGF) (75-100 mV/mm)
Macrophages (61)	- Migration towards anode (50-300 V/m) - Enhanced phagocytic uptake (50-150 V/m)
Neutrophils (57)	- Migrate towards cathode (50-100 V/m)

Recently, electroceuticals, which generate open circuit potentials due to the presence of dissimilar metals in contact with a conducting fluid, have become an emerging treatment modality as electrical stimulation wound dressings. Electroceuticals have

become commercially available with approval from the US Food and Drug Administration

(FDA) for infected wounds. These commercially available dressings, such as Arthrex®

and Procellera®, use the generated electric fields from the open circuit potential to help

generate electrochemical reactions in the wound bed but have no current flow (64). Bogie

et al. demonstrated their group's Modular Adaptive Electrotherapy Delivery System

(MAEDS) to reduce *Pseudomonas aeruginosa* loads within infected, porcine wounds.

MAEDS is a patented, disposable bandage that uses biphasic charge-balanced stimulation

to treat wounds on a 10% duty cycle (operating 6 minutes of every hour) (65). However,

the optimal electric stimulation parameters for MAEDS have yet to be investigated in

accordance with wound healing and the mechanisms responsible for wound healing and

bacterial load reduction have not been investigated apart from their device's similarity to

conventional wound electrotherapy (65, 66).

On the other hand, direct current (DC) has also been shown to have bacterial

inhibitory effects against both gram-positive and gram-negative bacteria (67, 68). The

printed electroceutical dressing (PED) has demonstrated the inhibition of *Staphylococcus*

aureus and *Pseudomonas aeruginosa* biofilms *in vitro* due to the generation of reactive

oxygen species (ROS), primarily hypochlorous acid (HOCl) (10, 11, 69). Additionally,

hydrogen peroxide (H_2O_2), which has shown to be an effective agent against *Pseudomonas*

aeruginosa (70), is likely produced by the PED (69). Moreover, the PED has demonstrated

efficacy *in vitro* to inhibit antibiotic-strains of *Pseudomonas aeruginosa* (10). While the

ability of the PED to inhibit bacterial biofilms *in vitro* suggests the understanding of some

antimicrobial mechanisms that may lead to chronic wound healing, the use of the PED *in vivo* has seen limited investigation (69).

In this thesis, Chapters 2 and 3 continue to investigate the use of DC to heal wounds by applying the PED to two animal chronic wounds and developing protocol for an uninfected murine wound model. Chapters 4 and 5 focus on the advancement of the PED into SPEEDs by increasing circuit flexibility, integrating a Bluetooth® circuit, and adding a third electrode for controlled treatment dosing.

Chapter 2: PED Intervention Treatment of Chronic Wounds*

In vivo, the PED was utilized in two clinical case studies as an experimental treatment for the therapeutic intervention on non-healing and chronically infected wounds. A four-year-old Mastiff underwent PED treatment after >1 year of open wound management, a free skin graft, and negative pressure dressings. A one-year-old domestic shorthair (DSH) cat underwent PED treatment after ~8 months of wound management, antibiotics, and skin flaps.

2.1 Materials and Methods

The printed electroceutical dressing (PED) fabrication and safe use has been previously reported (69, 71). Briefly, the fabric-based PED was constructed by screen-printing the medically compatible Ag/AgCl ink (Creative Materials #113-09) onto a habotai silk substrate (Figure 2A). The PED was powered by a 6 V battery with maximum current limited to 600 µA through a 10 kΩ ballast resistor. Medical tape encapsulates all electrical components while providing an electrical and fluid isolation layer, leaving the printed electrodes and battery pack accessible for use. The larger dressings (7.5 cm x 7.5 cm, Figure 2B and 2C) presented an interdigitated electrode layout that maximizes the anode area for highest bacterial clearance (10, 11). For cat wounds, a smaller PED (1 cm x 2 cm, Figure 2D and 2E) was used with simplified electrode geometry to match past *in vitro* bactericidal effects (10, 11).

For PED treatment, a hydrogel was first applied to the wound bed to ensure the PED electrodes were moistened when applied to the wound. The PED was then affixed

Parts of this chapter have been submitted as a short case series to Veterinary Surgery and is currently under review.

with additional bandages to the limb with the chronic wound so that the electrodes lay within the wound bed. A soft padded bandage was used to secure the PED to the dog chronic wound and a tie over bandage was used to secure the PED to the cat chronic wound.
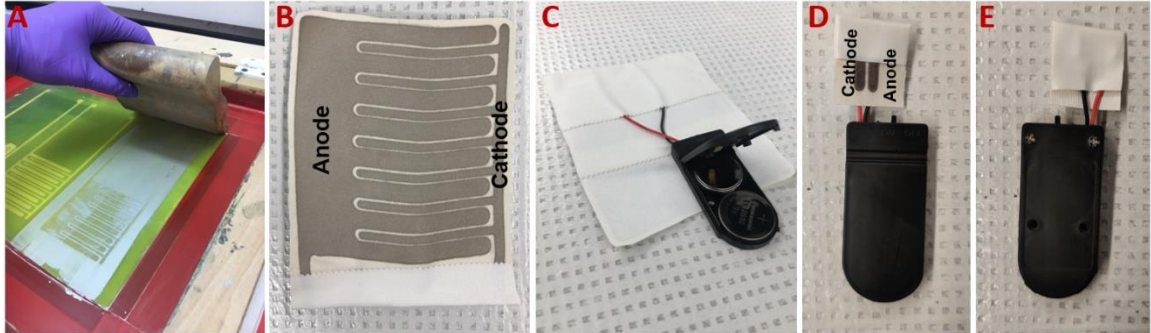
Figure 2. (a) The screen printing of the Ag/AgCl electrodes onto the PED silk substrate. (b) The 7.5 cm x 7.5 cm PED with the electrodes in an interdigitated design used for treating the dog wound. (c) The 7.5 cm x 7.5 cm PED is connected to a 6 V battery pack with circuit connections concealed with medical tape on the backside of the electroceutical dressing. (d) The 1 cm x 2 cm PED for smaller wounds used for the cat has geometrically simplified electrodes with equally sized anode and cathode. (e) As for the larger PED, the smaller PED was connected to a 6 V battery and concealed with medical tape. Both PEDs have a 10 kΩ ballast resistor limiting the current to 600 µA.

2.3 Wound Image Processing

Before each PED application, a digital photograph of the wound was captured with a ruler for reference. Each wound image captured was imported into MATLAB to determine the wound area using MATLAB's image processing toolbox (Figure 3) and compared to the pictured ruler for a length reference to determine wound area by pixel

10

count. To minimize user errors, wound area calculations were repeated three times and then

averaged and reported with the associated root mean square variance.
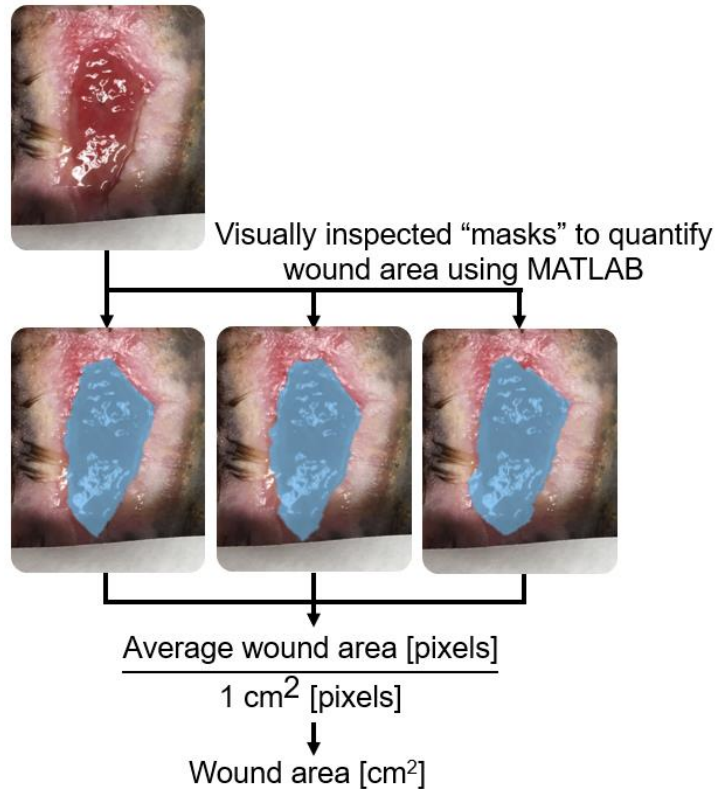
Figure 3. Process flow diagram showing the calculation of wound area. The blue areas were generated as "masks" for use with MATLAB to quantify the wound area using visual inspection. In each of these marked areas, pixels were counted to determine wound size. As these measurements rely on visual inspection, three measurements using independent masks were averaged and referenced to a ruler in the same plane as the wound to determine the wound size by pixel count.

2.4 PED Application in a Dog

A four-year-old female spayed Mastiff presented with a chronic wound on the distal

antebrachium that was caused by a bite wound with marked tissue infection. Prior to the

use of the PED, one year of treatments included open wound management, negative

pressure wound therapy, and skin grafting with 50% graft failure. Prior to the skin graft, a

11

punch biopsy was taken that showed antimicrobial insensitivity to several antibiotics (e.g.,

Amoxicillin, Ampicillin, Cefazolin, Cefpodoxime, Doxycycline,

Trimethoprim/Sulfamethoxazole, and Chloramphenicol). Following these treatments, the

patient was transferred to the primary care veterinarian for open wound management. One

year after the initial wounding event, a 4.2 cm^2 full-thickness wound was on the

distomedial aspect of the right antebrachium with pale white unhealthy granulation tissue

within the wound bed and peripheral fibrous tissue. The wound had minimal effusion.

Before PED application, the dog was sedated with intravenous butorphanol

(0.2 mg/kg) and dexmedetomidine (4 mcg/kg). The peri-wound skin was shaved and

cleaned with a chlorhexidine scrub (2%) and benzalkonium chloride (Zephiran). A 6 mm

punch biopsy of the center of the granulation tissue was conducted and revealed

Staphylococcus pseudintermedius and *Streptococcus canis* with antimicrobial insensitivity

to Ampicillin and Penicillin (Figure 4). Hydrogel (Skintegrity, Medline Industries, Inc)

was copiously applied to the granulation bed. A 7.5 cm x 7.5 cm PED (Figures 2B, 2C)

was applied to the wound and secured to the limb with a soft padded bandage. Four PEDs

were applied (initial dressing plus three dressing changes) over a 10-day treatment period

with the first PED application classified as day 0. The PED was changed two days

following initial application, and the wound was observed to decrease from 4.2 cm^2 to 3.2

cm^2. At the next dressing change four days later, wound area decreased from 3.2 cm^2 to 2.4

cm^2. After the last PED was removed on day 10, the wound area decreased to 1.0 cm^2

(Figure 5). The root mean square variance in the wound area for each measurement was ±0.08 cm^2.

CULTURE W/SUSC (MICRO) Verified on: 12/02/17

Spec#	Spec ID	Specimen	Isolate #	Organism	Amount
1		Wound	1	Staph pseudintermedius (s.pseud)	1 Colony
1		Wound	2	Streptococcus canis (s.canis)	1 Colony

Figure 4. The culture results from the punch biopsy of the Mastiff chronic wound before initial PED treatment.

A punch biopsy (day 6) of the tissue was performed and submitted for culture and antimicrobial susceptibility. No bacterial growth occurred after PED treatment for 6 days. Over the 10 days there was a ~4.2X reduction in the wound area. The dog was discharged for continued care with the primary care veterinarian for completion of second intention healing. The wound was covered with a non-adherent dressing (Telfa) and a soft padded bandage. No antibiotics were prescribed. A re-check was performed at the clinic 67 days later and showed complete healing of the wound (Figure 5; day 67 image).

Parts of this chapter have been submitted as a short case series to Veterinary Surgery and is currently under review.
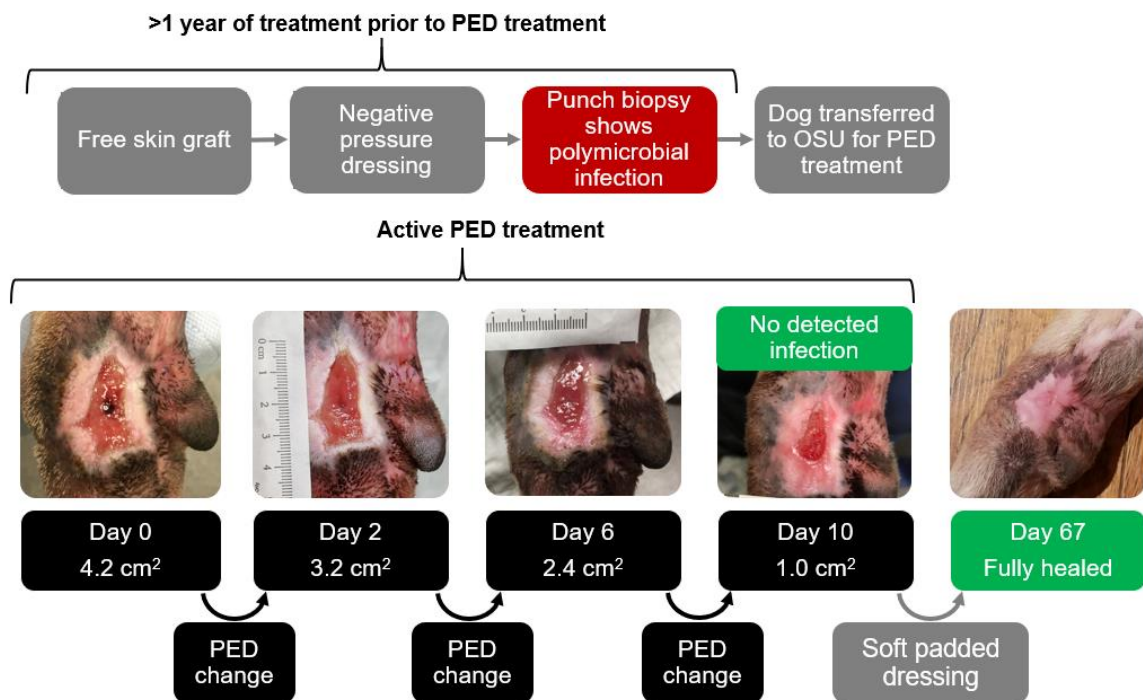
Figure 5. The figure represents a schematic summarizing the treatment prior and post-PED. Following the last PED treatment, a punch biopsy detected no infection. The canine was released to in-home care with no antimicrobials and a soft padded dressing. The wound showing to be fully healed 67 days after initial PED treatment. The root mean square variance each wound are measurement was ±0.08 cm^2.

2.5 PED Application in a Cat

A one-year-old, female-spayed domestic shorthair (DSH) cat presented with a full thickness wound extending from the left flank to the lateral stifle. Open wound management was performed until a healthy bed of granulation tissue was present as determined by the attending clinician. Five months after injury, an advancement flap was then used to close the defect. Three days following surgery, partial dehiscence of the wound occurred, and a wound culture detected *Pseudomonas aeruginosa*. The cat was treated with

14

pradofloxacin (5.5mg/kg PO q24h) with continued open wound management until a healthy bed of granulation tissue was re-established. Six months following the initial wounding, an interpolation flap was used to close the defect, and dehiscence of the distal 40% of the interpolation flap occurred 12 days post-operatively.

The wound remained static despite treatment. A wound biopsy was cultured and showed an eosinophilic granuloma complex (EGC) seven months following the initial wounding. The EGC was managed with prednisone (2mg/kg PO q24h) for the following month with open wound management. After that time, another biopsy revealed resolution of the EGC. Prednisone was tapered and discontinued over three weeks. The wound remained static (2.4 cm^2 wound area) despite open wound management, eight months following the initial injury.

After resolution of the EGC, another biopsy of the wound was cultured and showed *Staphylococcus epidermidis*. The cat was not on systemic antibiotics and no new antibiotics were initiated. At this time, hydrogel was applied to the wound bed and the smaller PED (Figures 2D, 2E) was applied. A tie over bandage was used to affix the bandage to the wound.

Prior to applying each PED, the cat was sedated with methadone (0.2 mg/kg), dexmedetomidine (10 mcg/kg), and ketamine (5 mg/kg) given intramuscularly. The peri-wound skin was prepped as previously described for the dog. A total of five PEDs over 17 days were used for the treatment course determined by wound evaluations with dressing changes every 3-6 days. The first PED change occurred after six days, and the wound area

15

decreased from 2.4 cm^2 to 1.7 cm^2. Four days later, a dressing change revealed the wound

at 1.6 cm^2. The next PED was applied three days later, showing the wound size of 1.3 cm^2.

The last PED change was four days later, and the wound area decreased to 0.9 cm^2 (Figure

6). The root mean square variance in the wound area for each measurement was ±0.03 cm^2.

A 2 mm punch biopsy was submitted for culture on day 17 and there was no bacterial

growth. Over the 17 days, wound area decreased by ~2.5X. Open wound management was

continued for another 6 weeks with hydrophilic foam (Covidien) as the primary layer until

complete re-epithelialization of the wound (Figure 6; day 47 image).
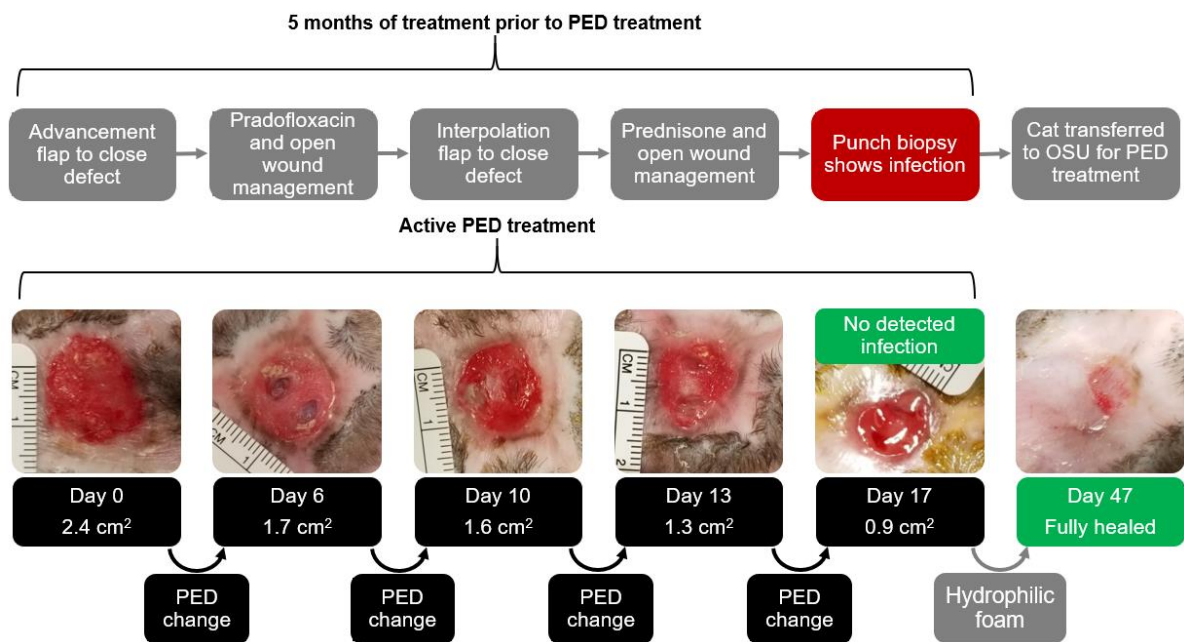
Figure 6. The figure represents a schematic summarizing the treatment prior and post-PED for the domestic short haired cat. The PED was applied and changed four times. Following the last PED treatment, a punch biopsy detected no infection. The cat was released to in-home care with the wound showing to be fully healed 47 days after initial PED treatment. The uncertainty for each measurement is less than ±0.03 cm^2.

16

2.6 Discussion

Prior to clinical use, efficacy of the PED for infection mitigation had been reported *in vitro* (10, 11, 69) and for safe operation in humans (71). The two cases presented here showed significant efficacy in eradicating persistent infections over a 10-day PED treatment course for the dog and a 17-day treatment course for the cat. Infection removal in both animals correlates to past *in vitro* results where 3-5 log reduction in bacterial CFU counts for 24-hour *Pseudomonas aeruginosa* and *Staphylococcus aureus* lawn biofilms treated with electroceuticals were reported (10, 11, 69). The PED, *in vitro*, generates reactive oxygen species, primarily HOCl (11), to mitigate bacterial infection. In both animals, no observations of host cytotoxicity were recorded. *In vitro*, the observed bacterial clearance occurs over the anode, motivating the enlarged anode area on the PED (Figure 2B). Less substantial inhibitory effects may take place over the cathode due to the electric potential favoring the production of H_2O_2 (70); however, the bacteria may be able to recover from the oxidative stress from H_2O_2 (72)- mediated disinfection.

Past *in vitro* results have reported eradication of antibiotic tolerant variants that may arise in cultures (10). The bacterial cultures from the dog tissue biopsies showed insensitivity to several antibiotics (e.g., Amoxicillin, Ampicillin, Cefazolin, Cefpodoxime, Doxycycline, Trimethoprim/Sulfamethoxazole, and Chloramphenicol) prior to the skin-graft surgery. Moreover, the wound after the skin graft failed with persistent infection (*Staphylococcus pseudintermedius* and *Streptococcus canis*) remaining resistant to

17

Ampicillin and Penicillin. The PED treatment resolved infection and demonstrated a continued reduction (~4.2X) in wound area over 10 days.

In many cases, the presence of *Staphylococcus epidermidis* is often dismissed (73); however, these bacteria have the capability to post-operatively hinder wound healing, like *Staphylococcus aureus* (74, 75). Investigations in murine wounds have shown that *Staphylococcus epidermidis* impairs healing by delaying re-epithelialization (76). Prior to PED treatment, the cat chronic wound showed the presence of *Staphylococcus epidermidis* following two skin-flap surgeries with dehiscence post-operatively. Despite the clearance of EGC within the wound after the second flap, *Staphylococcus epidermidis* persisted, and the wound remained static. However, after 17 days of PED treatment there was no detectable infection and the wound area decreased by 2.5X.

After various standard, established wound care treatments failed to resolve the chronic wounds on the dog and the cat, the PED proved to be an effective treatment in eliminating infections and led to complete wound healing. While the results of this study did show that PED treatment was effective in promoting healing in chronic wounds in both cases, there were some limitations. Notably, dosing of electrical stimulation parameters and treatment course was not consistent between the two cases. Therefore, the results here are limited to key observations. During the treatment course, there were no complications, adverse events, or side effects noted in either case. In both cases, long standing infection was resolved with reduction in wound area.

18

Chapter 3. Development of an Uninfected Wound Model for PED Evaluation

The printed electroceutical dressing (PED) has proven efficacy *in vitro* to inhibit bacterial biofilms (10, 69, 77) and *in vivo* to aid chronic wound healing where other methods have failed as presented in Chapter 2 (69). However, the role of the PED to aid in wound healing where infection is not present has yet to be investigated. As discussed in Chapter 1, electrical stimulation has been shown to have migratory and proliferation effects on a variety of host and host-immune cells. Keratinocytes and neutrophils have shown to migrate to the cathode (57, 78) under physiologically relevant magnitudes of electrical stimulation while fibroblasts and macrophages migrate to the anode (61, 62). Additionally, electrical stimulation has been suggested to promote angiogenesis through enhanced production of the vascular endothelial growth factor (VEGF) (63). Therefore, methods to evaluate the PED in an uninfected wound model must be developed in order to differentiate any pro-healing effects of the PED that are independent of mitigating infections.

Murine models are commonly used for *in vivo* chronic, non-healing wound models (79). Moreover, their relative low-cost compared to larger animal models and easy to maintain reputation makes for a desirable pilot study animal (80). First, the PED had to be scaled down for the size of a dermal injury typically introduced for mouse (< 10 mm critical dimension). Additionally, electrical operation parameters will likely need to be adjusted to minimize pain and discomfort to the subject. A two-mice study was utilized to evaluate the safety of the PED for mouse wounds. Next, a twelve-mice study was conducted as a pilot

study to identify pitfalls and protocol adjustments when comparing control and PED treatment groups.

3.1 Adapting the PED for Mice Studies

The original size of the PED (7.5 cm x 7.5 cm) was scaled down by reducing the size of the electrodes to fit within a mouse wound that was caused by a 6 mm punch biopsy. Across 24 wounds, the 6 mm punch biopsy creates wound areas of 28.7 ± 6.6 mm^2 on the back of a mouse. The PED was reduced to a 1 cm x 2 cm dressing with geometrically simplified electrodes (Figure 7) that would fit within a mouse full-thickness wound caused by the 6 mm punch biopsy. The geometrically simplified electrodes have proven efficacy previously *in vitro* (10, 11) and with the cat chronic wound intervention treatment reported in Chapter 2. The PED was reduced in weight to not restrict the movement of the mouse. The smaller 1 cm x 2 cm PED weighed 1.2 grams, a 14.3 grams reduction from the 7.5 cm x 7.5 cm PED. Most of this weight loss was due to the replacement of the commercial 6 V battery pack with a 1.5 V battery encased in heat-shrink wrap. A 270 kΩ resistor was placed in series with the battery for a comparable current density to that of the 7.5 cm x 7.5 cm PED. The current density through the 34.43 cm^2 anode of the larger PED was 1.74×10^{-5} A/cm^2 with the maximum current limited to 0.6 mA. The current density through the anode of the smaller PED was 2.33×10^{-5} A/cm^2 with the maximum current limited to 5.6 μA. The heat-shrink wrap acted as a case for the battery. Hot glue sealed the openings of the heat-shrink wrap to secure the wires in place and to create a watertight seal around the battery (Figure 6B). The exposed wires were then epoxied to the electrodes. Medical tape

(Band-Aid Water Block Tape) covered the epoxy connections and any remaining exposed

wire.
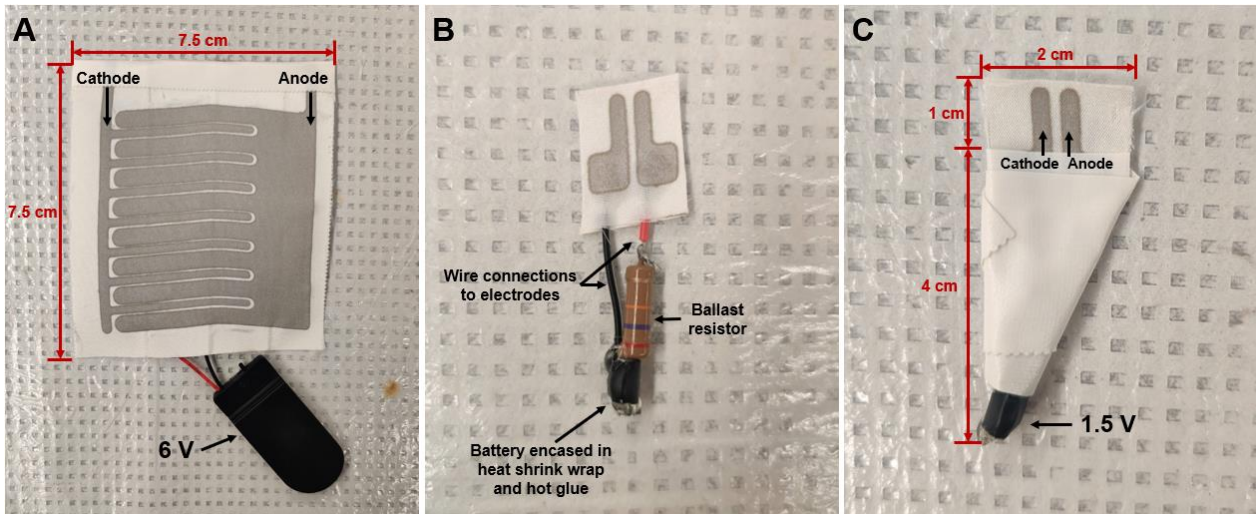
Figure 7. (a) 7.5 cm x 7.5 cm PED with an enlarged anode connected to a 6 V commercial battery pack. (b) The exposed circuit of the 1 cm x 2 cm PED before being concealed with medical tape to show the components of scaling down the circuit. (c) 1 cm x 2 cm PED that was adapted for placement on mice. A 1.5 V battery is concealed in heat shrink wrap and the circuit connections are sealed with medical tape.

3.2 Pilot PED Mice Study

To ensure the safety of the mice in further studies, two mice (C57BL/6) underwent

an evaluation study to determine the safety of the 1 cm x 2 cm PED. To be clear, this study

was not intended for evaluating the efficacy of the PED healing uninfected wounds.

Instead, the PED was evaluated for safety by two factors: weight and current. One mouse

was deemed the 'weight' mouse with the electrodes of the PED and comparable weight but

without a power source. This 'weight' mouse would be used to evaluate if the weight of

the smaller PED caused any pain or limited mobility. The 'current' mouse had the PED

with power, a 1.5 V battery and a 270 kΩ resistor that limited the maximum current to

5.6 µA that would be evaluated for mouse pain by observing any abnormal behavior of the mice.

Both mice were anesthetized using an isoflurane chamber at a rate of 2-5%. Buprenorphine was administered by IP injection for an analgesic, and both mice were shaved where the 6 mm punch biopsy tool was used to create two wounds on the back of the mice. Hydrogel (3M Tegaderm Hydrogel Wound Filler) was applied to both wounds on the mice and the PED under study was applied to the left-side wound, aligning the electrodes to be within the wound bed (Figure 8) The PED with no power was applied to the right-side wounds of both mice. A film dressing (Opsite Flexifix, Smith and Nephew) was used to secure the device to each mouse by wrapping it around the outside of the device and the body of the mouse (Figure 8). The two mice were placed in the same cage and underwent observation for three days after wounding and applying the dressings. No dressing changes were made.
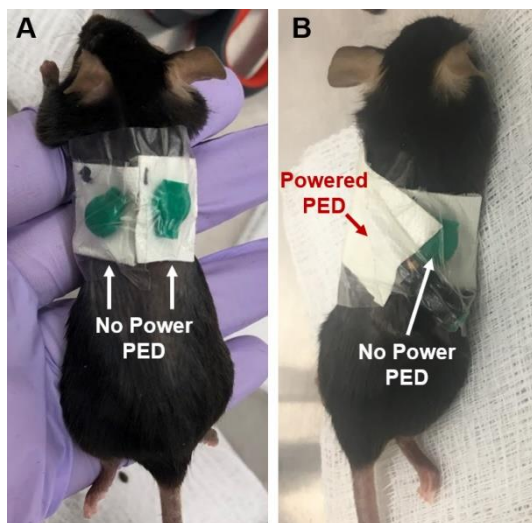
Figure 8. (a) C57BL/6 mouse with PEDs applied on both wounds that were not connected to power for electrodes only control. The 'no power' PEDs were of comparable weight to the powered PED. (b) C57BL/6 mouse with a PED connected to a 1.5 V battery and 270 kΩ ballast resistor on the left-side wound. A 'no power' PED is applied to the right-side for electrodes only control.

22

There was no observed discomfort of either mouse over the three days after wounding and applying the dressings. The current and weight of the adapted smaller PED was deemed safe to move forward with a larger pilot mouse study that would guide dosing parameters and establish protocol for evaluating the PED on uninfected wounds. While observations of the mice were promising to move forward, key adjustments needed to be made before transitioning to a larger study. First, even after shaving the mice, the hair on the mice proved to be an obstacle for visual observation of the wounds and posed challenges by making the medical tape difficult to remove from the hair on the mouse without tearing skin. Additionally, the wounds were observed to heal in irregular shapes that make manual measurements with a ruler imprecise. These pitfalls resulted in adjustments that were made before moving to the next study. The adjustments were to: (1) replace the C57BL/6 mice with SKH1-hairless mice and (2) standardize a picture taking process for image analysis of the wound area.

3.3 Pilot PED Protocol Mice Study

A twelve mice pilot study was used to develop an uninfected, mice study protocol that would lead to evaluating the efficacy of the PED to healing uninfected wounds in later *in vivo* studies. Different dosing parameters were used within groups of the mice to gain insight on the effect of PED dosing before moving to a larger, randomized evaluation for pro-healing effects of the PED.

3.3.1 Materials and Methods

As before, the 1 cm x 2 cm PED electrodes (Figure 7C) were utilized in this pilot study. 12 SKH1-hairless mice were used in place of the C57BL/6 mice. The 12 mice were split into three study groups (Figure 9). Two of the groups were PED treatment groups with the following circuit specifications: (T1) 1.5 V, 270 kΩ and (T2) 1.5 V, 27 kΩ. The third group was a control group (C) with the PED electrodes without connection to power. Each group had the respective PED placed on the right-side wound and the left-side wound was covered with a silk covering for an additional control wound on each mouse.
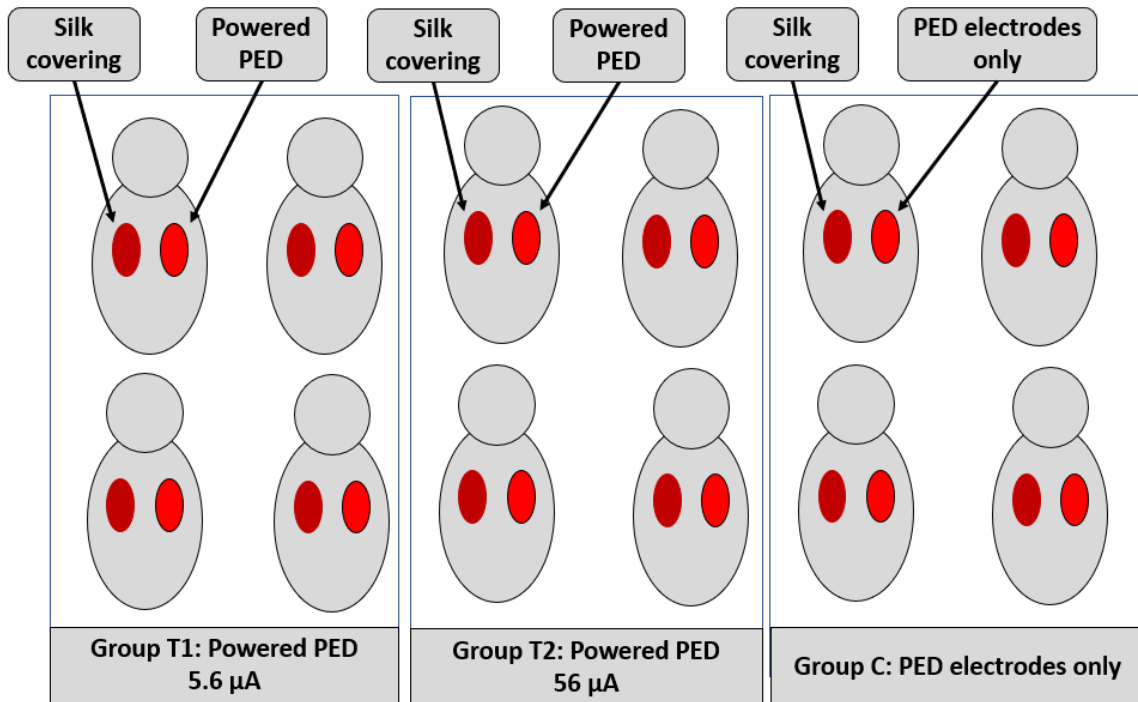
Figure 9. Each mice group contains four mice and silk coverings on the left-side wounds. Group T1 right-side wound has a PED connected to a 1.5 V battery and 270 kΩ resistor that limits the current to 5.6 μA. Group T2 right-side wound has a PED connected to a 1.5 V battery and a 27 kΩ resistor that limits the current to 56 μA. Group C right-side wound has a 'no power PED' that has a comparable weight to the powered PEDs, but no power source connected to evaluate the effect of the electrodes alone.

The SKH1-hairless mice were anesthetized using an isoflurane chamber at 2-5%, and Buprenorphine was administered by IP injection for an analgesic. Using a dermal punch biopsy tool, a 6 mm full-thickness dermal wound was created on the back of the mouse, creating two wounds. To simulate the application of a wound dressing not being applied immediately after wounding and to allow the wound to stabilize, the mice were wounded, and the wound was left exposed with no covering for one day. The PED was applied to each group the next day, designated as Day 0. To apply the PED, the mice were anesthetized using an isoflurane chamber at 2-5% and hydrogel (3M Tegaderm Hydrogel Wound Filler) was applied to both wounds on the mouse. Following, the PED was applied to the right-side wound and silk was applied to the left-side wound. The dressings were secured to the mouse by film dressing (Opsite Flexifix, Smith and Nephew) that wrapped completely around the mouse's back and belly without limiting movement (Figure 10A). Each group was housed in a cage together between dressing changes (Figure 10B).
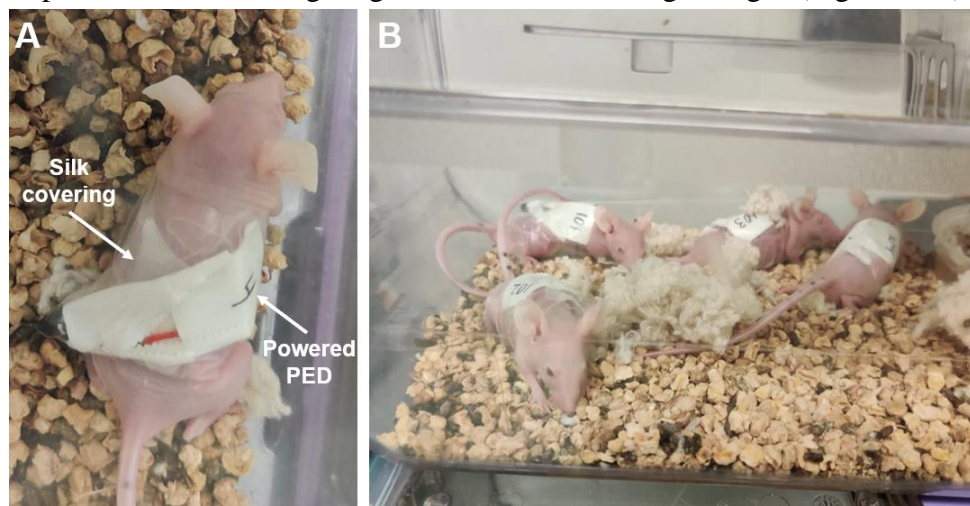
Figure 10. (a) SKH1-hairless mouse with the powered PED applied to the right-side wound and a silk covering on the left-side wound. The dressings were secured with film dressing. (b) One group of four mice housed in a cage together between dressing changes.

The same procedure for applying the dressings took place for each dressing change: each mouse was anesthetized, and the dressing was removed from the mouse carefully to ensure no tearing of the skin. Images were captured of every wound each time the dressings were changed. Then, hydrogel was reapplied to each wound and the PED was replaced on the right-side wound and the silk was replaced on the left-side wound with tape securing the dressings. Figure 11 displays the timetable for changing the PED. Dressing changes took place on Days 2 and 4. Three days following the last dressing change (Day 7), final wound pictures were captured before the mice were euthanized and the wound bed tissue was harvested for histology and further staining to confirm that the time point of tissue harvesting was appropriate.
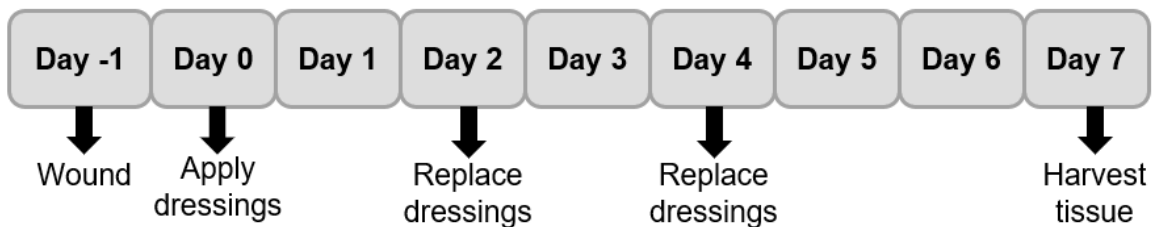
Figure 11. The figure shows the protocol for wounding the mice and applying the PED. The mice were wounded, and the dressings were not applied until one day layer, Day 0. The dressings were replaced on Day 2 and 4, and the study concluded on Day 7.

3.3.2 Wound Image Processing

The wound image processing protocol presented in Chapter 2 was repeated for this pilot study. Before each PED application, a digital photograph of the wound was captured with a ruler for reference. The replacement of the C57BL/6 mice with SKH-1 hairless mice allowed for clear imaging of the wound without hair visually impairing a picture for image processing. Each wound image captured was imported into MATLAB to determine the

wound area using MATLAB's image processing toolbox and compared to the pictured ruler for a length reference to determine wound area by pixel count. To minimize user errors, wound area calculations were repeated three times and then averaged.

3.3.3 Results and Discussion

Digital photographs of the wounds on Day 0 revealed that the punch biopsy did not create uniform-sized wounds on each mouse. Day 0 wounds were 28.7 ± 6.6 mm^2, determined by MATLAB as previously described. To quantitatively evaluate the healing progression of each wound, the wound on a day (Day X) under analysis is compared to the Day 0 area of that wound and wound closure is calculated as shown in (1).

$$\text{Wound Closure (\%)} = \frac{\text{Wound area Day 0-Wound area Day X}}{\text{Wound area Day 0}} \times 100\% \qquad (1)$$

For comparison between treatment wounds and the silk covered wounds, the difference between the wound closure percentage is calculated as shown in (2). A positive difference in wound closure represents increased closure in the treatment wound over the closure in the silk covered wound.

$$\text{Difference in Wound Closure(\%)} = \text{Treatment Wound Closure(\%) - Control Wound Closure(\%)} \qquad (2)$$

Throughout the study, there were pitfalls that prevented the three mouse groups from being directly compared. The PED and silk that was applied to the back of the mice did not always remain on the mice for the 24 hours before a dressing change due to a mixture of adhesive failures, the mice chewing on the film dressing, and the rigidity of the PED restricting the amount of film dressing that could be applied to the mouse's body. Therefore, many wounds were exposed to the environment for different amounts of time, possibly causing additional scabbing or drying of the wound compared to wounds that

stayed covered. However, when a mouse wound was uncovered within the 24 hours before a dressing change, it was observed that the entire group (T1, T2, or C) wounds were uncovered with the exception of two mice on Day 4 in group T2 that retained their dressings while the other two mice dressing came off. To account for the potential different times when the dressing was off the wounds, the wound closure difference between the treatment wound and silk covered wound on each mouse was calculated then averaged with standard deviation reported in addition to the reported wound closure (%).

Group T1 mice were treated on the right-side wound with a PED connected to a 1.5 V battery and 270 kΩ resistor that limited the maximum current to 5.6 μA. These circuit specifications are consistent with the pilot PED study with two mice in Section 3.2 that did not cause the mice pain or discomfort. The left-side wound was covered with silk. The dressings in Group T1 stayed on the mice except between Day 6 and Day 7, where every mouse had removed the dressings. Figure 12 shows the progression of wound healing by wound closure (%) across the seven-day study and difference in wound closure (%) between the 5.6 μA PED treated wound and the silk covered wound.
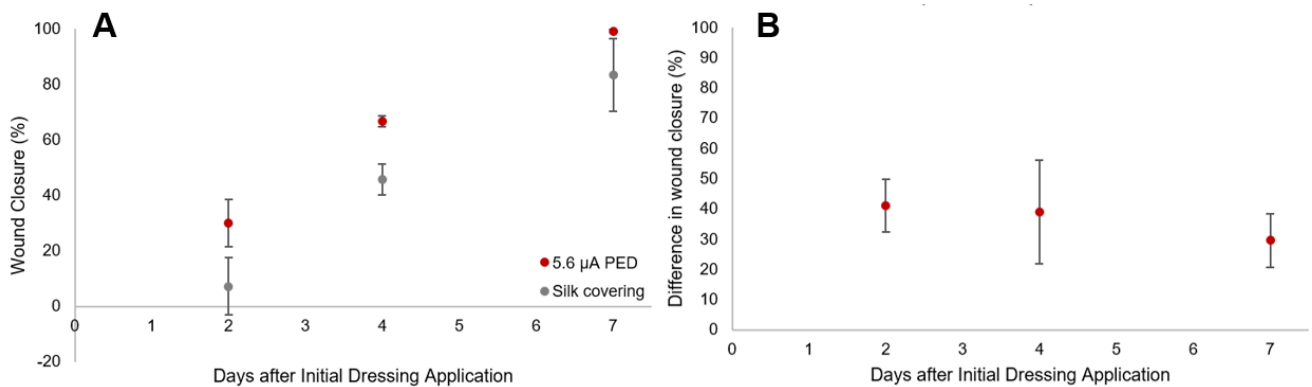
Figure 12. (a) Wound closure (%) for the treatment wound and the silk covered wound for T1: 5.6 μA PED (b) The difference in wound closure between treatment wound and the silk covered wound. A positive percentage indicates a higher closure of the treatment wound.

28

The 5.6 µA PED consistently produced higher rates of wound closure than the silk only covering. On days 2, 4, and 7, the 5.6 µA PED treated wound had an increased closure in wound over the silk covered wound by 41%, 39%, and 30%, respectively (Figure 12B). The PED treated wounds also had a smaller variance in wound area across the four mice than the silk covered wounds on day 2, 4, and 7 as shown in Figure 12A. The wound area and percent decrease for each wound is listed in Appendix A.

Group T2 mice were treated on the right-side wound with a PED connected to a 1.5 V battery and 27 kΩ resistor to limit the maximum current to 56 µA. This is a 10X increase in current but lies beneath reported currents applied to mice for electrical stimulation (81). The left-side wound was covered with silk. The dressings and coverings on the mice in Group T2 came off the mice in the 24 hours before the Day 4 dressing change and within 24 hours of Day 7 when the tissue was harvested. Figure 13A shows the wound closure (%) for the 56 µA PED treated wound and the silk covered wound. Figure 13 B shows the difference in wound closure between the 56 µA treated PED wound and the silk covered wound.
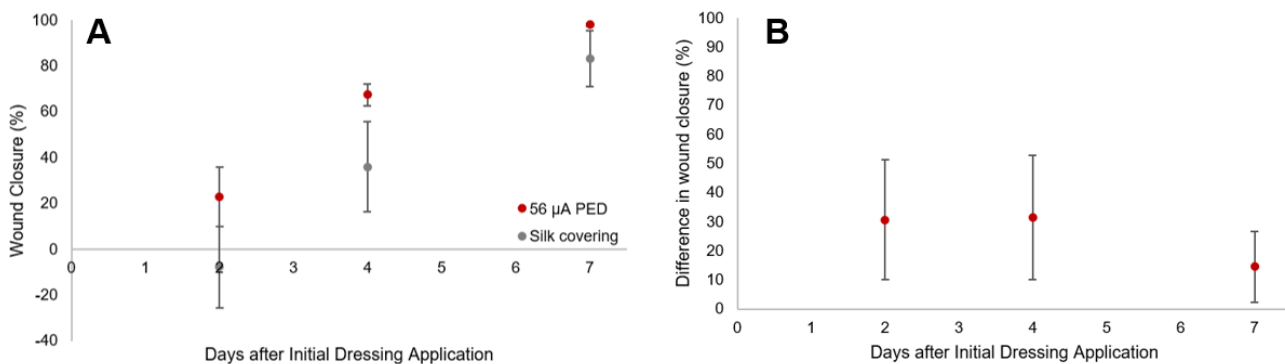
Figure 13. (a) Wound closure (%) for the treatment wound and the silk covered wound for T2: 56 µA PED (b) The difference in wound closure between treatment wound and the silk covered wound. A positive percentage indicates a higher closure of the treatment wound.

29

The 56 µA PED used with Group T2 produced higher wound closure rates compared to the silk covering for the four mice. The 56 µA PED had increased wound closure over the silk covered wound on days 2, 4, and 7 by 31%, 31%, and 15%, respectively. Additionally, there was more variance in wound closure rates in the silk covered wounds on days 4 and 7.

Group C mice had the right-side wound treated with a PED that was not connected to a power source, to evaluate the influence of the Ag/AgCl electrodes without a current flow. The left-side wounds were covered with silk. The wounds dressings came off the mice in the 24 hours before Day 2 and Day 7. Figure 14A shows the right-side wound closure from the 'no power' PED and the left-side wound closure from the silk covering across the seven-day study. Figure 14B shows the difference in wound closures between the electrodes only treated wound and the silk covered wound.
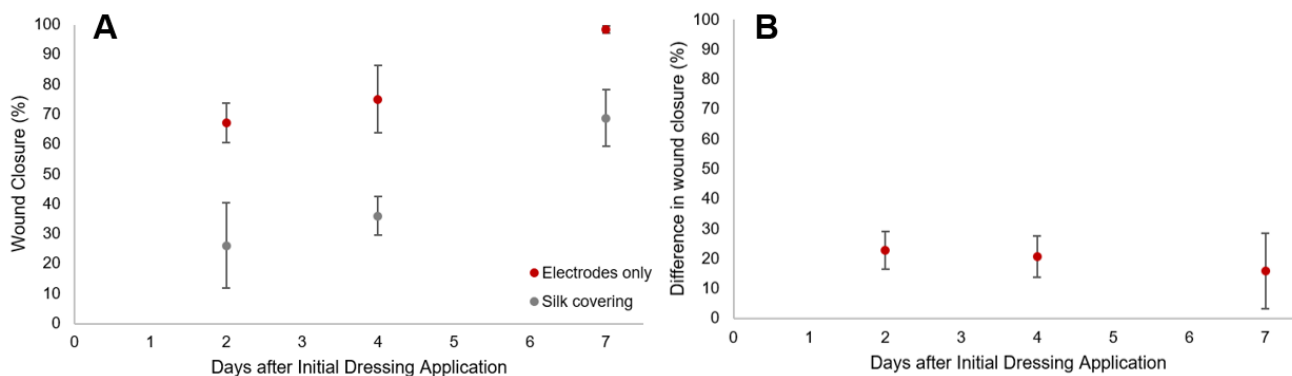
Figure 14. (a) Wound closure (%) for the treatment wound and the silk covered wound for C: Electrodes only (b) The difference in wound closure between treatment wound and the silk covered wound. A positive percentage indicates a higher closure of the treatment wound.

Group C wounds with the electrodes only PED consistently had a higher wound closure rate than the silk covering. On days 2, 4, and 7, the electrodes only treated wound

had higher wound closure over the silk covered wounds by 23%, 21%, and 16%, respectively. The wound size and percent decrease in wound area for each day and mouse wound is tabulated in Appendix A.

Across all three study groups, the PED or electrodes consistently increased wound closure rate in comparison to the silk covering. As discussed previously, cross-group comparisons cannot be made due to the dressings falling off the mice inconsistently across the groups (Table 6,8,10 in Appendix A). An intragroup comparison may make for a more viable comparison as the dressing were observed to fall off within 24 hours before a dressing change within an entire group. The only exception to this were two T2 mice that retained the dressings on while two T2 mice had dressings come off on day 4. The mice group with the electrodes only (no power PED) had all four mice without dressings within 24 hr before day 2. Additionally, the mice with the 56 µA PED treatment had two of the four dressings come off within the 24 hr before day 4. Across all three mice groups, every dressing came off within the 24 hr before day 7, the final day of the study. Moreover, there was a variety of engineering and biological pitfalls of the pilot mouse studies that must be addressed to produce a viable, uninfected murine wound protocol.

First, the PED under evaluation was placed on the right-side wound on every mouse. To ensure that there is no wound location bias, the PED or electrodes under study should alternate between the left and right sides of the mice. Alternating the side that the dressing is placed on should eliminate healing dependence on any unforeseen anatomical factors and variations in wound size per side due to the nature of punch biopsy wounding.

31

Additionally, all mice in the two pilot studies were female. To eliminate the sex of the mice as a variable, both male and female mice should be included in further studies.

From an engineering perspective, improvements to the PED and how it is secured to the mouse must be made. The dressings must be fully secured to the mouse between dressing changes for comparisons across study groups to made. Not only does the dressing falling off impact the PED dosing treatment, but the wound exposure to open air can cause the wound to dry out or scab over and influence wound closure (82, 83). The adhesive wrap used on the mice shows evidence that a mixture of mouse chewing and failure of the adhesive results in the dressings coming off the mice. Alternative securements must be able to hold the dressings in place across multiple days and not restrict the movement of the mice. Rodent jackets have been used previously to secure devices to mice (84), but further research must be done to validate the use of jackets with the PED.

Finally, the size and rigidity of the mouse-adapted PED also creates difficulties when securing the device to the wounds on the mice. While the electrodes on the PED are an appropriate size for the wound, the circuit and circuit connections to the electrodes make up a majority of the size (Figure 7C). Moreover, the rigidity of the circuit makes securing the device a challenge. The rigid, coin battery that is used for the PED is bulky on the back of the mouse and creates difficult connections that elongate the PED. A conformable power source would allow for a fully flexible PED and simplify device securement.

Chapter 4: Flexible Battery

The shortcomings and pitfalls of the mice study exposed room for improvement within the PED system. Rigidity of the circuit, specifically the battery, limits the conformability of the dressing. Figure 15 shows the 4 cm elongation of the mouse-adapted PED with the rigid circuit and connections, as well as the 6 V rigid, commercial battery pack in use for the 7.5 cm x 7.5 cm dressing.
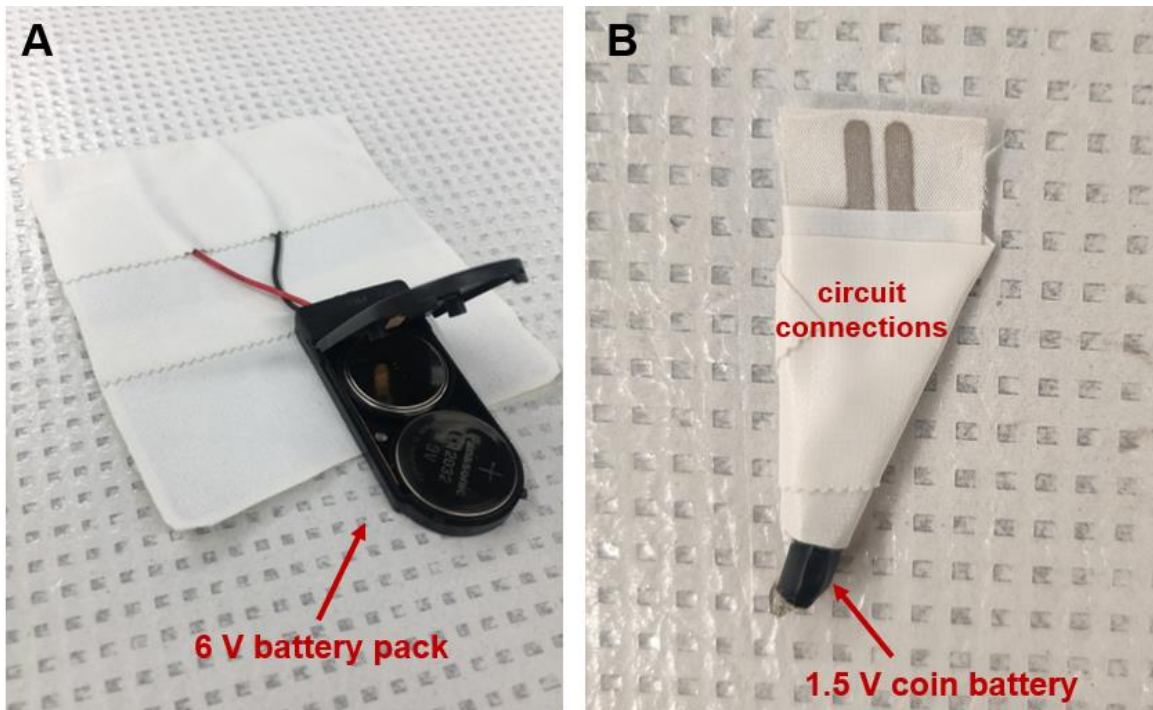
Figure 15.   (a) The 6 V rigid, commercial battery pack on the 7.5 cm x 7.5 cm electroceutical dressing. (b) The 1.5 V rigid coin battery used for the mouse-adapted electroceutical with the circuit connections creating additional elongation.

Within the mouse study, the battery and circuit connections made it difficult to secure the dressing to the mice. The circuit connections in the mouse-adapted PED elongate the device whereas the circuit connections for the 7.5 cm x 7.5 cm PED are concealed on the backside of the electrodes. Moreover, the 6 V commercial battery pack utilized with

the 7.5 cm x 7.5 cm PED is a bulky, weighted component that hangs off the silk dressing and requires additional securement. Therefore, a flexible, conformable battery to replace the rigidity of commercial batteries is preferable for the transition from the PED to SPEEDs. In this chapter, the beginning work of a biofluid-wetted, flexible battery is reported.

4.1 Introduction and Previous Work

Recently, flexible batteries have become a point of investigation due to electronic wearables becoming increasingly popular for activity and health trackers. Flexible batteries for health monitoring patches have been shown with success (85), but are based in PDMS and hydrogel to match their fully integrated system. Few textile batteries have been demonstrated but the batteries either contain numerous materials that would add significant cost to SPEEDs (86) or have not shown viable integration within a flexible system (87, 88).

For a viable, flexible battery to be integrated into SPEEDs, a similar fabrication process is desired. Various printing techniques have been proven to be a viable method to deposit metallic inks for the fabrication of flexible batteries. Screen printing, ink-jet printing, flexographic printing, and gravure printing are optimal techniques for substrates such as paper, plastic, or textile to enable low-cost, high throughput fabrication (89–94). Utilizing similar fabrication processes and materials to the PED, screen printing a silver-zinc flexible battery allows for the use of fabrication materials already present within the system such as the silk substrate, screen printing apparatus, and Ag/AgCl ink.

Silver-zinc batteries were first developed in the 1950s and found success due to their high specific energy along with their reliability and safety in comparison the Li-ion batteries (95, 96). Moreover, silver-zinc batteries provide low environmental risks that allow silver-zinc to be utilized as primary batteries in a disposable system (97). Many of the first applications were used for large systems in space or underwater, such as a 256-ton silver-zinc battery for the Albacore G-5 submarine (95). However, more recently, silver-zinc batteries have found success as flexible (85, 98) and stretchable (99) power sources. Therefore, this work leads to the development of a flexible, fabric-based, silver-zinc battery that will be integrated with the SPEEDs in further work.

To evaluate a new flexible battery system that can be integrated with the PED, traditional electrochemical techniques are used to test the performance of the battery and optimize electrode compositions. Electrochemical impedance spectroscopy (EIS) is a common technique used to investigate the distinctive impedance signature of each electrode in the cell and the charge transfer processes. This electrochemical technique measures the impedance of the cell while sweeping across a range of frequencies to give a signature of ohmic resistance, capacitance, and diffusion (100). Another common technique is to run charge-discharge curves. Due to the disposability of SPEEDs, the silver-zinc flexible battery will be a primary battery (not rechargeable), and therefore will only require a discharge curve for characterization. This testing measures the capacitance of the cell and gives insight into how the battery performs under various load conditions (100).

Given that this is the first evaluation and attempt to improve the fundamental system comprising the PED, the electrochemical techniques presented in this chapter are

limited to cyclic voltammetry (CV). CV is an electrochemical technique that sweeps across a potential range, first in the positive direction and then in the negative direction, while measuring the resulting current for each potential. The scan rate at which the potential is swept can influence the magnitude of output current due to the change in diffusion layer of the reaction species. Scan rates can also positioning of anodic and cathodic peaks, and give insight into the reversibility of the electrochemical cell (101). In this work, we use cyclic voltammetry to confirm the reaction mechanisms the cell is using, particularly at the Ag/AgCl electrode to confirm the two silver charge transfer mechanisms (presented in Section 4.2) before further electrochemical techniques are used. The remainder of this chapter focuses on the operating principle behind the flexible battery, fabrication process, CV, and scaling the voltage for SPEEDs integration.

4.2 Silver-Zinc Battery Operating Principle

The flexible battery uses a silk substrate to match the conformability of SPEEDs. The wound fluid that may flow through the SPEED electrodes is absorbed by the flexible battery silk substrate and acts as an electrolyte for the electrochemical redox reaction that can be harnessed as direct current (DC) power (Figure 16).
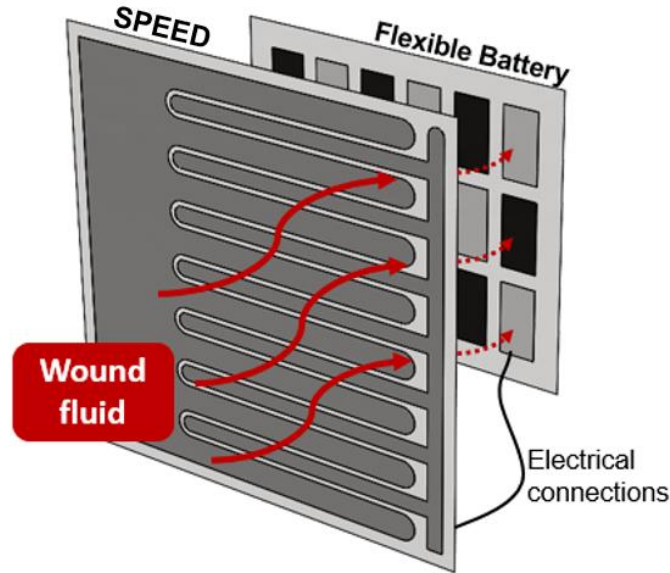
Figure 16. The flow of would fluid from the wound bed, through the SPEEDs electrodes and to the flexible battery.

A silver-zinc composition of the flexible battery allows for the use of the same Ag/AgCl ink (Creative Materials #113-09) that composes the SPEEDs electrodes. The Ag/AgCl acts as the cathode when coupled with a zinc electrode, the anode. When an ionically conductive medium connects the cathode and anode, a reduction-oxidation reaction occurs and produces a potential difference between the two electrodes that can be harnessed. Silver may be reduced by two discharge processes (102), as shown in (1) and

(2), and the silver chloride in (3). Meanwhile, zinc is oxidized at the anode as described in (4).

$$2AgO + H_2O + 2e^- \rightarrow Ag_2O + 2OH^- \quad (1)$$

$$Ag_2O + H_2O + 2e^- \rightarrow 2Ag + 2OH^- \quad (2)$$

$$AgCl + e^- \rightarrow Ag + Cl^- \quad (3)$$

$$Zn + 2OH^- \rightarrow Zn(OH)_2 + 2e^- \quad (4)$$
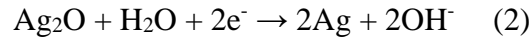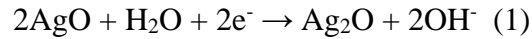
To use the electric potential from this electrochemical reaction, current collectors are be connected to the electrodes. Wires can be used as current collectors and give access to measuring the electric properties of the electrochemical cell. If one were to measure the voltage difference of the cell, the resulting measurement would read the potential difference between the silver cathode and the zinc anode, also known as the open circuit potential. However, for current to flow, the circuit must be completed by connecting the silver-zinc couple to SPEEDs or another finite load. At this point, electrons would flow through the electrolyte to counteract the imbalance of potentials at the cathode and the anode (Figure 17), and therefore, power SPEEDs.
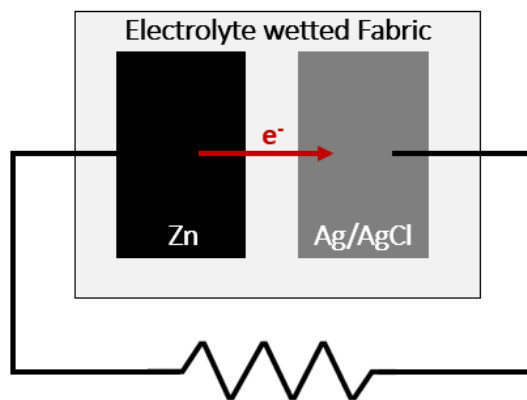
Figure 17. When the Ag/AgCl cathode and Zn anode are wetting with an electrolyte and connected to a finite load, electrons flow from the anode to the cathode to balance the potentials.

38

The battery pack currently in use for the PED runs 6 V while the smaller, 1 cm x 2 cm PED uses 1.5 V for power in the mouse study. To obtain comparable voltages, the redox reaction described above can be placed in series. Moreover, larger amounts of silver and zinc can increase the capacity of the flexible battery, creating a system that can be built specifically for the desired application. The remainder of this chapter demonstrates the beginning work of tailoring a flexible battery for SPEEDs operation.

4.3 Fabrication

To keep the fabrication materials to a minimum in SPEEDs, flexible battery is screen-printed and uses the same habotai silk substrate (Jacquard Ink-Jet Printing Silk Sheets) and Ag/AgCl (Creative Materials #113-09) ink utilized for the SPEEDs electrodes that are placed on the wound. To create a screen-printed zinc electrode, a zinc ink was made in-house. The ideal zinc ink would have a viscosity that allowed for screen printing and use a minimal amount of zinc without a significant drop in open circuit voltage when paired with its silver cathode counterpart.

The zinc ink consists of zinc dust (<10 μm), polyvinyl alcohol (PVA), and dimethyl sulfoxide (DMSO). PVA is used as an inexpensive filler to limit zinc material, as well as for its emulsifying and adhesion properties. DMSO is a non-toxic solvent that dissolves both polar and nonpolar compounds, aiding in the dissolution of PVA. To determine the appropriate ratios of Zn:PVA:DMSO, the weight percent of Zn and PVA was varied for testing, while DMSO was added until an appropriate viscosity for screen-printing was

achieved. To form the zinc ink, the DMSO is added to a glass beaker on a hot plate at 80°C

with a stir bar (100 rpm). The PVA is slowly added (0.5 g/min) and left to dissolve in the

DMSO for 30 minutes. The zinc is then slowly added (0.5 g/min) and left to stir for an

additional 5 minutes. Table 3 displays the trials of the recipes and their respective open

circuit voltage measurements.

Table 3. The trials of creating a zinc ink with minimal zinc material and appropriately
viscosity for screen printing. The green shaded row is the recipe that was chosen for the final
zinc ink.

Zinc (wt%)	PVA (wt%)	DMSO (wt%)	Open Circuit Voltage
68%	8%	24%	0.9 V
58%	14%	28%	0.9 V
45%	19%	35%	0.9 V
34%	23%	44%	0.9 V
31%	8%	61%	0.9 V
27%	27%	46%	0.8 V
11%	26%	63%	0.7 V

As evident in Table 3, the weight percent of zinc, PVA, and DMSO at 31:8:61,

respectively, maintained the open circuit voltage of 0.9 V with the lowest weight percent

of zinc until the open circuit voltage dropped in value. The weight percent ratios work to a

recipe of 4 grams of Zn, 1 gram of PVA, and 7 mL of DMSO to produce a small batch of

screen-print capable ink.

To fabricate a full cell of the flexible battery, two screen designs were created in

Solidworks, one for each electrode print, with registration marks to align the designs for

consistent electrode spacing (Figure 18). For simplicity, a single cell consists of one block

print of zinc and one block print of silver. The screen design allows for nine cells to be

printed at once. The full print of the screen is 5.8 cm x 4.6 cm, designed to fit on the back

of the 7.5 cm x 7.5 cm SPEEDs with additional space for remaining circuit components.
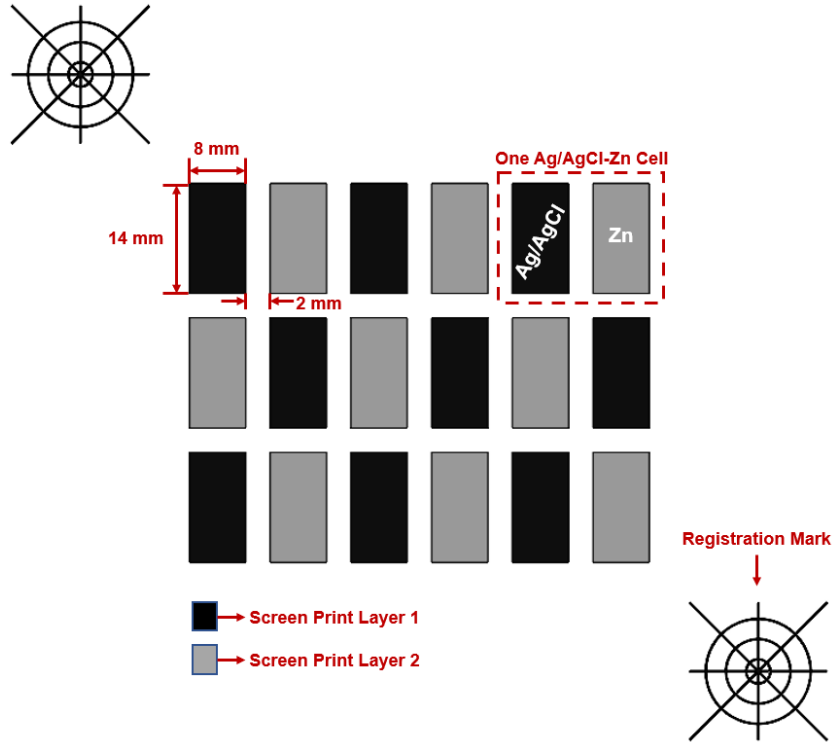
Figure 18. The screen design layers made in CAD for the printed, flexible battery. The black print is the first screen print design that is printed. The gray color indicates the second screen print design that is printed after the first ink is cured and realigned under the screen. Registration marks on the corners is used to realign the print and keep spacing consistent between the cells.
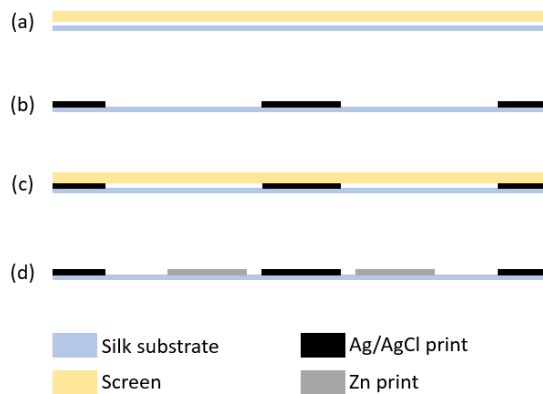
Figure 19. (a) The screen-print screen is placed over the silk substrate for Ag/AgCl ink deposition. (b) The resultant cured Ag/AgCl print (c) the screen is realigned using registration marks for Zn ink deposition. (d) The resultant prints after the Zn ink is cured

41

First, Ag/AgCl ink is screen printed onto a silk substrate then cured on a hot plate at 100°C for 10 minutes (Figure 19A, 19B). The zinc ink is prepared as previously described and after aligning the second screen design to the cured Ag/AgCl print by the registration marks, the zinc ink is screen printed (Figure 19C, 19D). The zinc is then cured on the hot plate at 100°C for 10 minutes. Figure 20 shows SEM images of the two metal prints. The screen-printed, cured Ag/AgCl ink shows complete coverage of the silk substrate. However, the screen-printed, cured Zn ink does not fully cover the silk substrate and silk fibers are visible in the SEM image. The electrical discontinuity of the Zn print was confirmed by a voltmeter.
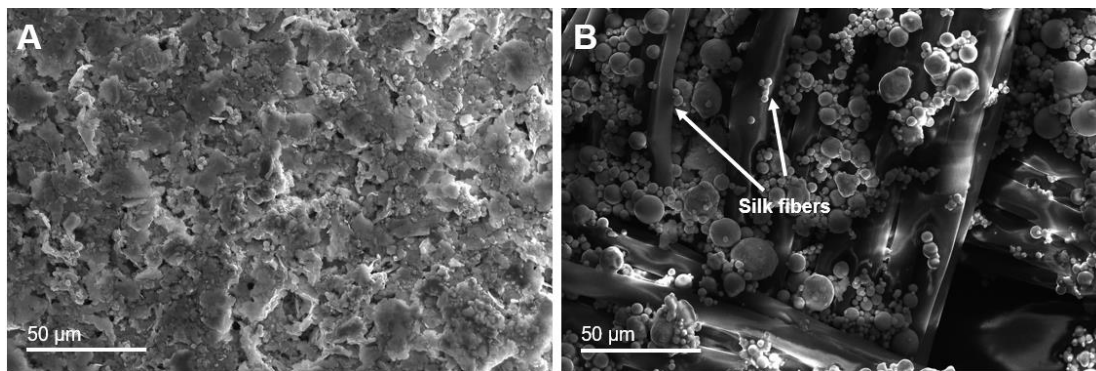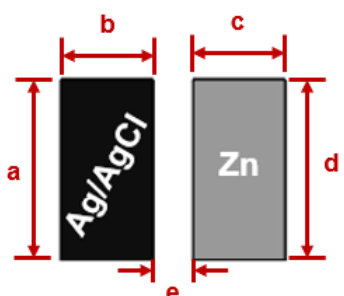
Figure 20. (a) SEM image of the top view of the screen-printed, cured Ag/AgCl ink overtop the silk substrate. (b) SEM image of the top view of the screen-printed, cured Zn ink overtop the silk substrate. Arrows indicate the silk fibers that are not fully covered by the Zn print.

The nominal and printed dimensions of the Ag/AgCl-Zn cells vary as shown in Table 4. The widths (b and c) of the blocks are designed to be 8 mm each with a 2 mm space between the electrode prints. When printed, the Ag/AgCl block width is reduced to 7 mm and the Zn block width is consistent with the design width at 8 mm. The spacing between the blocks (e) is 2.5 mm. The lengths (a and d) of both blocks are designed to be

14 mm. The Ag/AgCl print is consistent with the 14 mm length while the Zn print is 15 mm.

Table 4. Summary of the design versus printed dimensions of the Ag/AgCl-Zn cell.

Dimension	Design	Printed
a	14 mm	14 mm ± 0.5 mm
b	8 mm	7 mm ± 0.5 mm
c	8 mm	8 mm ± 0.5 mm
d	14 mm	15 mm ± 0.5 mm
e	2 mm	2.5 mm ± 0.5 mm

After screen-printing and curing the Ag/AgCl and Zn inks, each cell is cut apart so that a hydrophobic barrier may be placed between each cell in series to scale voltage. Without a hydrophobic barrier between the cells, each cell would be connected in parallel instead of in series, and the voltage would not increase. To assemble a flexible battery of more than one cell, the cells are adhered to medical tape, with a 2 mm strip of medical tape between each cell as a hydrophobic barrier. The cells are then connected in series by silver epoxy and conductive thread, a more flexible option than wiring. The first and last cells in the series are then epoxied to wires for circuit connections to be made to the cathode and anode of the battery.

4.4 Cyclic Voltammetry

To evaluate the charge transfer mechanisms of the Ag/AgCl-Zn flexible battery, cyclic voltammetry (CV) was performed on one Ag/AgCl-Zn cell with 1X PBS as the

electrolyte to mimic the properties of biological fluid. CV was run with scan rates of 120

mV/s, 140 mV/s, 160 mV/s, and 320 mV/s. Multiple scan rates were chosen to show the

change in the diffusion layer from the electrode surface (Figure 21). The electric potential

began at -2.6 V, turning directions at +2.6 V to encapsulate the peaks of silver and zinc

reactions mentioned in Section 4.2 (98). From 0 V to 2.6 V, the reduction reactions at the

silver cathode and the oxidation reaction at the zinc anode will be indicated by peaks in

current. From 0 V to -2.6 V, peaks in current will represent the same reactions occurring

in the reverse reaction, meaning oxidation reactions at the silver cathode and reduction

reactions at the zinc anode. For a battery, this can give insight into the ability to discharge

and charge.
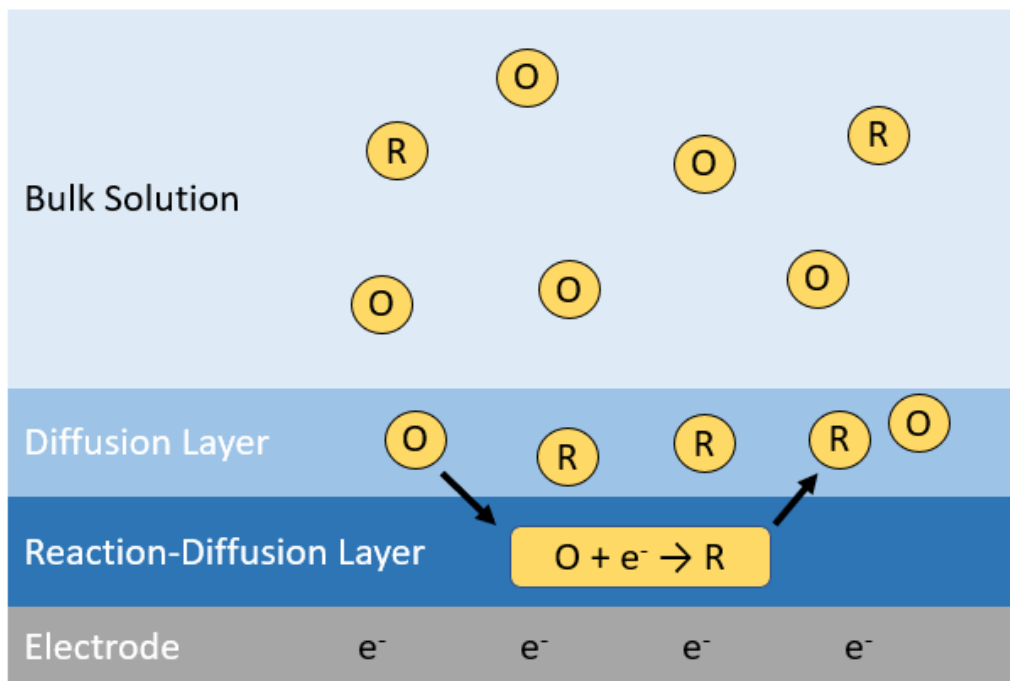
Figure 21. A schematic of the flow of a half reaction that takes place at the electrode surface. The reactant (O) diffuses to the electrode where the electron is added to product the product (R) that must then transports through the diffusion layer to the bulk solution.

Figure 22 shows the four cyclic voltammograms at different scan rates. The current peaks shift as the scan rate changes, indicating an irreversible system. Additionally, the peaks are not symmetric around the zero-potential axis, once again displaying the irreversibility of the system, specifically due to the lack of oxidation occurring at the silver cathode and reduction occurring at the zinc anode visible in the 0 V to -2.6 V range. As shown in Figure 22D, this correlates to an inability to recharge the battery after being discharged.
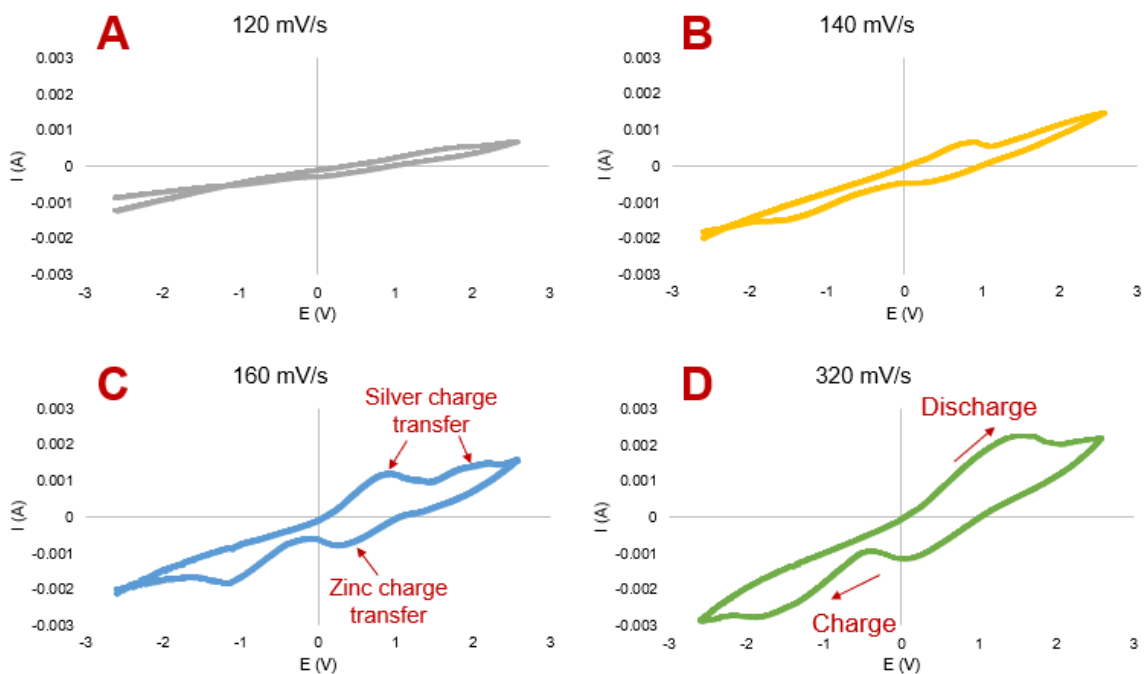
Figure 22. Cyclic voltammograms of the Ag/AgCl-Zn cell at scan rates of (a) 120 mV/s, (b) 140 mV/s, (c) 160 mV/s, and (d) 320 mV/s. The potential was swept from -2.6 V to +2.6 V, forward and in reverse.

At a scan rate of 160 mV/s (Figure 22C), the two anodic peaks representative of the two silver mechanisms within the electrochemical cell are distinguishable, following previously reported silver-zinc battery charge transfer mechanisms (98). The cathodic peak shown represents the zinc charge transfer mechanism. This CV confirms that the Ag/AgCl

cathode that is being used in place of a Ag or Ag_2O cathode still operates on the same operating reactions shown in Section 4.2.

4.5 Voltage Scaling for SPEEDs

To demonstrate the efficacy of the flexible battery, SPEEDs must be evaluated for its bacterial killing effect while connected to the flexible battery and compared to the performance of SPEEDs when compared to the rigid, commercial battery pack. However, the flexible battery must first produce high enough voltages to produce reactive oxygen species (ROS). The electric potential of 1.138 V applied to the SPEEDs electrodes produces ROS species (10, 77). This voltage can be obtained by connecting multiple Ag/AgCl-Zn cells in series.
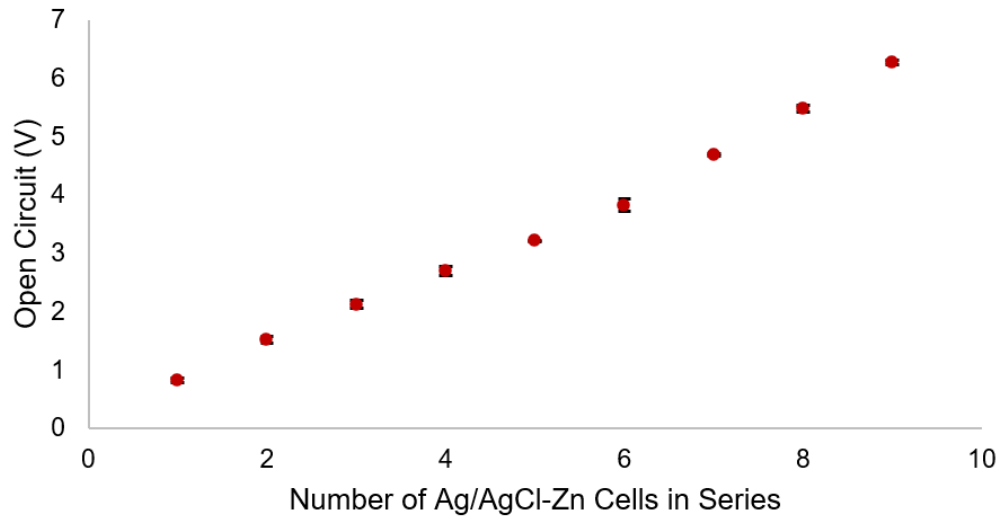
Figure 23. The scaling of open circuit voltage measurements when Ag/AgCl-Zn cells are placed in series. Up to nine cells in series is reported.

Figure 23 shows the scaling voltage of connecting Ag/AgCl-Zn cells in series. For each cell added, the voltage increases nearly linearly at ~0.67 V. A single cell produces an open circuit voltage of 0.81 V ± 0.04 V. Two cells in series produce an open circuit

46

voltage of 1.52 V ± 0.05 V, a large enough potential to produce HOCl and comparable to the 1.5 V rigid battery used for the mouse adapted PED. Nine cells (the number of cells in one screen print) produces an open circuit voltage of 6.27 V ± 0.04 V when connected in series, comparable to the 6 V commercial, rigid battery pack. Fully reported cell voltages are reported in Appendix B.

To demonstrate the ability of the voltage to scale for future implementation of the flexible battery with SPEEDs, nine cells were connected in series as a proof-of-concept design for the flexible battery (Figure 24). Each cell was placed on the adhesive side of waterproof medical tape, with 2 mm medical tape barriers in between each cell to hydrophobically isolate each cell. The cells were connected by conductive thread and silver epoxy. The cells on the ends of the series were then epoxied to wires so that a connection to SPEEDs could be made.
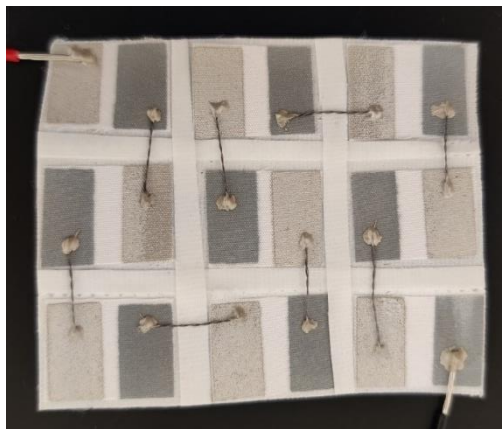
Figure 24.   Proof-of-concept design flexible battery. Nine Ag/AgCl-Zn cells are connected in series with silver epoxy and conductive thread and connected to wires on the anode and cathode of the full system for integration with SPEEDs.

The proof-of-concept design connected to SPEEDs the same as the commercial battery pack. Figure 25 demonstrates the connection to the SPEED in an *in vitro* setting. In this proof-of-concept evaluation, the flexible battery will be wetted outside by supplying 7 µL/min 1X PBS, simulating both the flow and electrolyte characteristics of wound fluid (103). Further design work must be done to fully integrate the flexible battery for *in vivo* settings. However, the ability to connect and evaluate the efficacy of the flexible battery to perform at the same level of the rigid, commercial battery pack *in vitro* shows promise to develop a fully flexible, integrated system.
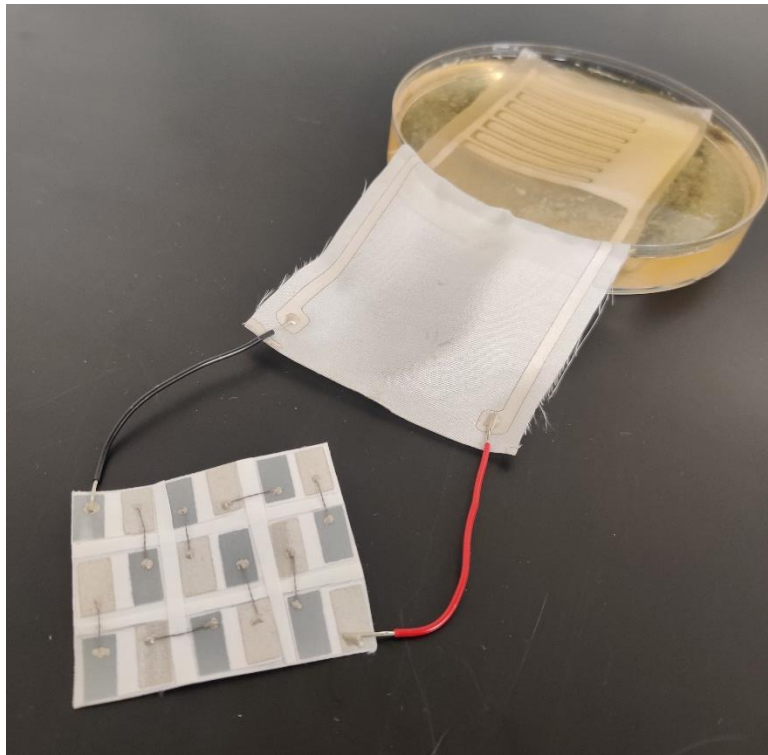
Figure 25. The proof-of-concept flexible battery design connected to the PED *in vitro* by silver epoxy and wires.

Chapter 5: Three-Electrode SPEEDs and Bluetooth® Integration*

In addition to a flexible circuit, improvements must be made to the PED to transform it into a smart platform with sensing capabilities and precise dosing. In this chapter, we demonstrate the capability of a three-electrode SPEEDs to control electrode potential and current dosing, as well as preliminary *in vitro* results for integrating a Bluetooth® circuit with SPEEDs.

5.1 Two- and Three-Electrode System

Currently, the SPEED exists as a two-electrode system. However, the two-electrode system presents limitations in controlling the potentials between the two electrodes despite being connected to a constant power source. The flow of current between the two electrodes makes it difficult to maintain a constant electrode potential. A lack of control over the electrode potentials results in a lack of control over the electrochemical reactions and products. Therefore, the reactive oxygen species (ROS) produced by SPEEDs may not be supplied at a steady rate and concentrations of the electrochemical products may vary within the wound bed throughout SPEEDs treatment.

To investigate the electrochemical reactions and ROS produced by the two-electrode SPEEDs, cyclic voltammetry (CV) of the SPEED within a soft tissue agar assay was performed (Figure 26). The electric potential sweep started at -2 V and switched sweeping direction upon reaching +2 V at a scan rate of 200 mV/s, a rate that would produce distinguishable cathodic and anodic peaks. It has been previously reported that at

49

an applied electrode potential of 1.138 V, HOCl may be generated as the primary ROS (104). At an applied potential of -0.6 V, H_2O_2 is produced (70). The flow of current present at these two potentials with our system shows that by altering the electrode potential, we can control the ROS produced.
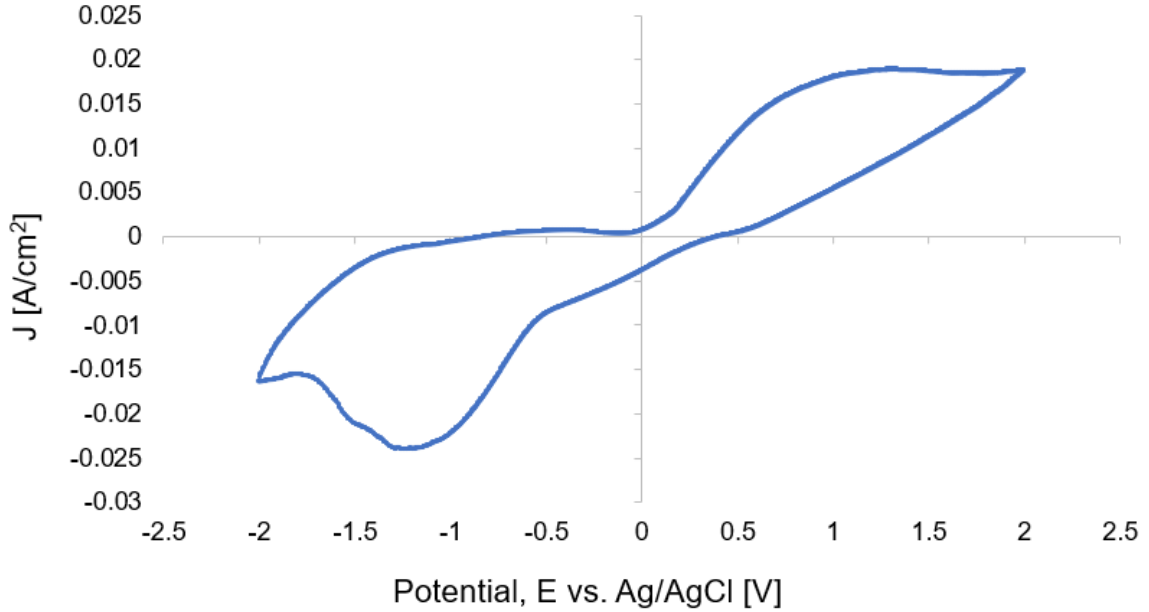
Figure 26. Cyclic voltammogram of the two-electrode PED embedded in the soft tissue agar gel to evaluate the products of the electrochemical products. The cycle had a starting potential of -2 V and a switching potential of +2 V at a scan rate of 200 mV/s.

The maximum and minimum current peaks present in Figure 26 are asymmetric in their magnitudes with the anodic peak at 0.019 A/cm^2 at an applied potential of 1.23 V while the cathodic peak is -0.024 A/cm^2 at an applied potential of -1.24 V. This asymmetric shape to the CV profile indicates that the electroceutical treatment of biofilms grown on agar is electrochemically irreversible i.e., non-Nernstian (101). The irreversibility indicates that the concentration of species needed to produce ROS are the limiting steps for the electrochemical reaction rates and not the transport of the species to and from the electrodes. Due to this non-Nernstian response, cyclic voltammetry is not an ideal

50

technique to quantitatively evaluate HOCl concentrations even though the actively flowing current measured indicates the production of the ROS at their respective potentials (101).
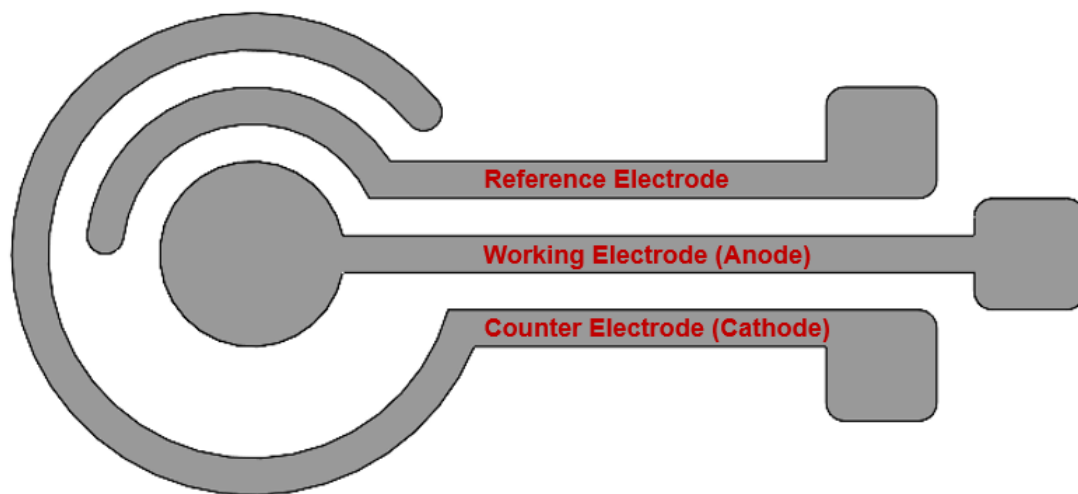
Figure 27. The preliminary three-electrode design. The working electrode acts as the anode and the counter electrode acts as the cathode.

To systematically control the electrochemical products, a third electrode was added to the system to act as the reference electrode. A preliminary design for the three-electrode SPEEDs system is shown in Figure 27. The anode acts as the working electrode where the desired potential is applied, and where bacterial clearance where primarily occur from the production of HOCl. The cathode acts as the counter, or auxiliary, electrode where current flows with the working electrode. The reference electrode has no current flow and is used to measure and control the potential of the working electrode. To investigate the electrochemical reactions and ROS produced by the three-electrode SPEED, cyclic voltammetry (CV) of the three-electrode system was performed as described for the two-electrode system (Figure 28).

51

Similar to the two-electrode system, the electric potential sweep started at -2 V and switched sweeping direction upon reaching +2 V at a scan rate of 100 mV/s. Due to the higher magnitude of the current peaks within the three-electrode system, a slower scan rate was able to observe additional profile characteristics, such as the diffusion regime shown in Figure 24. It is also evident within Figure 24 that the current flow at 1.138 V and -0.6 V shows production of HOCl and H_2O_2, respectively. The anodic peak is 0.039 A/cm^2 at an applied potential of 0.964 V. The cathodic peak is -0.049 A/cm^2 at -1.32 V applied potential.
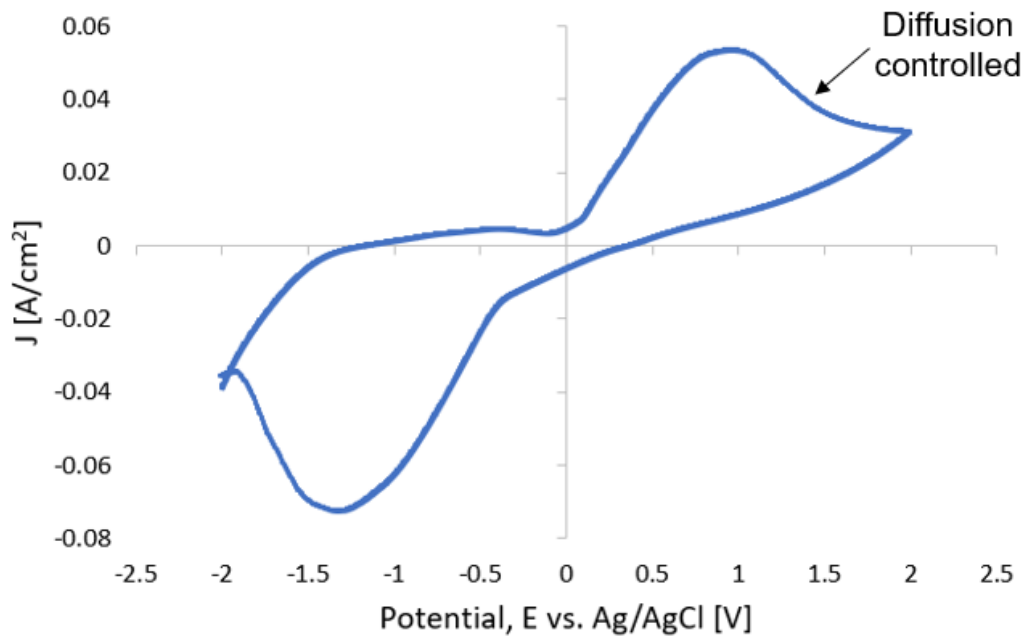
Figure 28. Cyclic voltammogram of the three-electrode PED embedded in the soft tissue agar gel to evaluate the products of the electrochemical products. The cycle had a starting potential of -2 V and a switching potential of +2 V at a scan rate of 100 mV/s.

Figure 28 indicates the diffusion-controlled regime, represented by the fall of current after the anodic peak at 0.964 V. This fall in current is due to the diffusion controlled delivery of the electrochemical products from the electrode surface to the bulk

52

solution. The rate at which the reaction takes place is limited to the rate at which reactants can reach the electrode surface by diffusion This contrasts with the two-electrode system where there was no evidence of the fall of current after the anodic peak, indicating that the rate of electrochemical products produced was reaction dependent. This change observed in the rate limiting step demonstrates the ability of the three-electrode system to produce ROS at rates that will not be altered by electrode interface, but instead by the diffusion of the species.

5.2 Bluetooth® Integration

Current, established clinical practice requires frequent visual inspections of the wound to determine healing outcomes. The visual inspections are generally carried out by trained medical professionals adding significant work burden to the practice of wound management, especially for chronic wounds. In this section, we report on a potentially new way to assist clinicians by allowing remote monitoring of the wound site. Since the SPEED is an electroceutical dressing with active electrodes, SPEEDs provide an opportunity to reduce the need for visual inspections and provide quantitative wound healing metrics. Therefore, a new physical biomarker is proposed for healing. It has been shown that the 'skin battery' creates current flow once the skin is wounded (53). Therefore, the trend of current flow through the wound can be measured as the resistance through the wound changes (i.e., the skin barrier is restored) as evident by Ohm's law ($V = iR$). Dry and unbroken skin behaves as an insulator high resistance construct to flow of electrical current with reported resistance ranging from 10 kΩ to 1 MΩ (105, 106).

*This chapter has been partially reported in Heald et al. *JMEMS.* 2020.
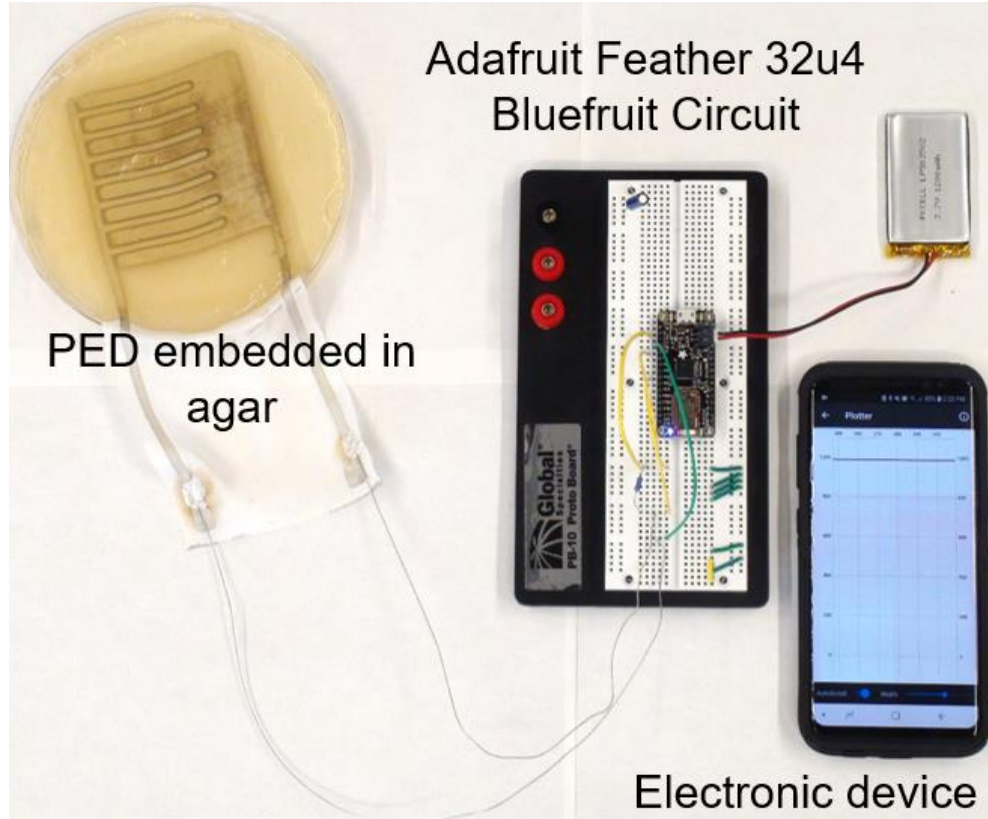
Figure 29. The capability of the PED to be connected to a Bluetooth® circuit for wound monitoring. The PED was embedded in the agar gel to measure the current flow via the Bluetooth® circuit with the data read out displayed on the electronic device (cellular phone).

An initial *in vitro* test with the soft tissue assay demonstrated Bluetooth® integration of SPEEDs with an Adafruit Feather 32u4 Bluefruit that records and transmits up to 20 ft real-time current monitoring (Figure 29). An Arduino IDE was used to measure the voltage drop across a known ballast resistor (10 kΩ). This measure voltage drop was pushed out *via* Bluetooth®, on the Adafruit Feather 32u4, to an Android application for a readout on a mobile phone. The reported current was post processed for a calculated current through the ballast resistor. The internal resistance of the Bluetooth® enabled monitoring

54

circuit is lower than the resistance of the agar gel assay during a direct measurement leading

to a higher recorded current than when measured directly (Figure 30) using an ammeter

due to the direction connections with shorter, silver wires for the Bluetooth enabled circuit.

However, the trend over time is the same and may be sufficient for real-time measurements

of the flow of current through the wound bed as the wound heals.
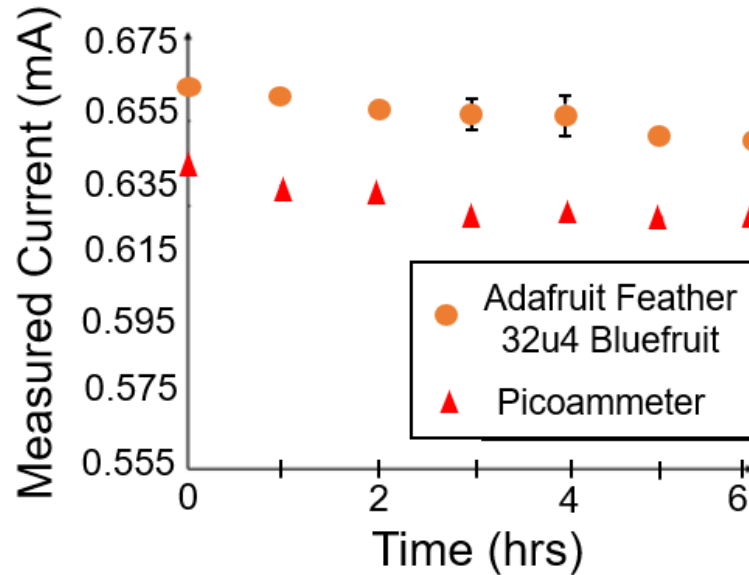
Figure 30. The Adafruit Feather 32u4 Bluefruit module with Arduino IDE and picoammeter current measurements recorded over time while the PED was embedded into the agar gel.

55

Chapter 6: Summary, Conclusions, and Future Outlook

In summary, chronic wounds present a major healthcare and financial burden on both human and animal populations. Moreover, chronic wounds pose many scientific and engineering challenges to heal chronic wounds and quantitatively evaluate wound healing. The printed electroceutical dressing (PED) has been proven *in vitro* to inhibit biofilms, even those that are resistant to antimicrobials (10, 11). However, the transition to a smart platform for engineered electroceutical dressings (SPEEDs) allows for the integration of sensors for wound evaluation and controlled treatment dosing. This thesis presented the beginning work of developing SPEEDs while continuing to evaluate the operational functionality of the electroceutical to heal chronic wounds. Continued work must be done to develop SPEEDs into a fully flexible system with integration of sensors and controlled dosing.

6.1 Summarized Findings

This thesis displayed the efficacy of the PED to heal chronic wounds as a clinical intervention treatment where other methods have failed. A four-year old Mastiff with a chronic wound that contained a polymicrobial infection was fully healed 67 days after initial PED treatment. This followed >1 year of established wound care involving a free skin graft and negative pressure dressing that failed to close the wound or eliminate infection. Moreover, the PED eradicated the infection after ten days. A DSH cat underwent

eight months of treatment that resulted in a static wound prior to PED intervention. The cat chronic wound fully healed after 47 days.

The efficacy of the PED to inhibit bacteria has been shown both *in vitro* and *in vivo* but work to evaluate the PED's ability to influence wound healing without infection has not been implemented. This work used two pilot mice studies to develop methodology that will be implemented in future *in vivo* uninfected wound models. Additionally, the pilot studies revealed biological and engineering pitfalls. Specifically, the device must be placed on both the left and right wounds to eliminate any location bias, the securement of the PED to the mice must be improved for cross-group comparison, and the rigidity of the PED must be improved.

A replacement of the rigid, commercial battery pack currently in use for the PED has been presented. The fabrication of a conformable, silver-zinc battery is demonstrated with an in-house, screen-printable zinc ink. The Ag/AgCl ink currently used for the electrodes makes a viable silver cathode, limiting the materials needed to implement this flexible battery. Additionally, the flexible battery voltage is easily scaled by placing the cells in series with hydrophobic barriers between the cells. It was shown that two cells in series creates an open circuit voltage comparable to the 1.5 V battery used for the mouse-adapted PED. Moreover, nine cells in series creates an open circuit voltage comparable to the 6 V battery pack in use for the 7.5 cm x 7.5 cm PED.

Lastly, this thesis demonstrated the ability to control the dosing metrics of SPEEDs by adding a third electrode to control the production of ROS with a stable electric potential.

SPEEDs also have the capability to be integrated with a Bluetooth® circuit that will allow for wound sensing capabilities in future work.

6.2 Future Work

The PED has been used as intervention treatment for two clinical case studies, but an *in vivo* study with mice allows for variable control for evaluating the efficacy of the PED to heal infected and uninfected wounds. Additionally, murine models allow for tissue harvesting at time points throughout the study before full wound healing. The tissue samples can be stained for select host immune cells to further the understanding of wound healing with the PED. Specifically, the PED's influence on inflammatory cells may be a point of interest as chronic wounds are believed to be wounds in a prolonged phase of inflammation (107). Additionally, this investigation into inflammatory cell influence may be extended to *in vitro* studies with electric fields equivalent to that of the PED to explore migration or proliferation in response to the electric stimulation.

Significant work must be done to fully integrate the flexible battery with SPEEDs. A separating layer between the flexible battery and the SPEEDs needs to be integrated and allow for wound fluid transport while maintaining hydrophobic isolation between each cell. Additionally, flexure testing on the battery should be conducted to ensure that the battery operates without short circuiting due to failure of hydrophobic barriers or the zinc and silver/silver chloride electrodes coming into contact with each other. EIS and discharge curves should be conducted to fully characterize the capability and limitations of the silver-zinc battery. Currently, the zinc electrode is not electrically continuous, possibly leaving material unused and limiting the life of the battery. Work is currently being done to alter

the zinc electrode and add current collectors that will allow for full use of the electrode materials and therefore, extend battery life.

Finally, the work presented here with the three-electrode system and the integrated Bluetooth® circuit were conducted *in vitro* and requires full integration with SPEEDs. While the CV of the three-electrodes displays the advantages compared to the two-electrode system, the size and shape of the three-electrodes should be optimized for bacterial clearance and minimal reference electrode interference. Additionally, the circuity to control the potentials with a feedback loop must be integrated. The Bluetooth® circuit integration was also completed *in vitro* without full implementation into the stand-alone SPEEDs. Further investigation into the metrics and sensing elements that can be integrated with the Bluetooth® should be conducted. This involves determining the metrics that may be clinically relevant to wound healing and evaluating if commercial sensors can be integrated or need to be developed in-house. In conclusion, there must be a joint effort to clinically evaluating the functionality of SPEEDs and to improve the sensing capabilities of SPEEDs to precisely heal wounds and evaluate wound healing.

References

1. Nunan R, Harding KG, Martin P. Clinical challenges of chronic wounds: Searching for an optimal animal model to recapitulate their complexity. DMM Dis Model Mech [Internet]. 2014 Nov 1 [cited 2021 Feb 10];7(11):1205–13. Available from: https://pubmed.ncbi.nlm.nih.gov/25359790/

2. Martin P, Nunan R. Cellular and molecular mechanisms of repair in acute and chronic wound healing [Internet]. Vol. 173, British Journal of Dermatology. Blackwell Publishing Ltd; 2015 [cited 2021 Feb 10]. p. 370–8. Available from: https://pubmed.ncbi.nlm.nih.gov/26175283/

3. Han G, Ceilley R. Chronic Wound Healing: A Review of Current Management and Treatments [Internet]. Vol. 34, Advances in Therapy. Springer Healthcare; 2017 [cited 2021 Feb 10]. p. 599–610. Available from: https://pubmed.ncbi.nlm.nih.gov/28108895/

4. Siddiqui AR, Bernstein JM. Chronic wound infection: Facts and controversies. Clin Dermatol [Internet]. 2010 Sep [cited 2021 Feb 10];28(5):519–26. Available from: https://pubmed.ncbi.nlm.nih.gov/20797512/

5. Metcalf DG, Bowler PG. Clinician perceptions of wound biofilm. Int Wound J. 2016 Oct 1;13(5):717–25.

6. Bowler PG. Antibiotic resistance and biofilm tolerance: A combined threat in the treatment of chronic infections. J Wound Care [Internet]. 2018 May 2 [cited 2021 Feb 10];27(5):273–7. Available from: https://pubmed.ncbi.nlm.nih.gov/29738295/

7. Bowler P, Murphy C, Wolcott R. Biofilm exacerbates antibiotic resistance: Is this a current oversight in antimicrobial stewardship? [Internet]. Vol. 9, Antimicrobial Resistance and Infection Control. BioMed Central Ltd; 2020 [cited 2021 Feb 10]. p. 162. Available from: https://aricjournal.biomedcentral.com/articles/10.1186/s13756-020-00830-6

8. Sen CK, Gordillo GM, Roy S, Kirsner R, Lambert L, Hunt TK, et al. Human Skin Wounds: A Major and Snowballing Threat to Public Health and the Economy. 2010;17(6):763–71.

9.   Markets and Markets [Internet]. Animal Wound Care Market. 2020 [cited 2021 Mar 23]. Available from: https://www.marketsandmarkets.com/Market-reports/animal-wound-care-market-253831778.html

10.   Lochab V, Jones TH, Dusane DH, Peters CW, Stoodley P, Wozniak DJ, et al. Ultrastructure imaging of Pseudomonas aeruginosa lawn biofilms and eradication of the tobramycin-resistant variants under in vitro electroceutical treatment. Sci Rep [Internet]. 2020 Dec 1 [cited 2021 Feb 5];10(1):1–12. Available from: https://www-nature-com.proxy.lib.ohio-state.edu/articles/s41598-020-66823-y

11.   Dusane DH, Lochab V, Jones T, Peters CW, Sindeldecker D, Das A, et al. Electroceutical Treatment of Pseudomonas aeruginosa Biofilms. Sci Rep [Internet]. 2019 Dec 1 [cited 2021 Feb 4];9(1):1–13. Available from: https://www.nature.com/articles/s41598-018-37891-y

12.   Swanson EA, Freeman LJ, Seleem MN, Snyder PW. Biofilm-infected wounds in a dog. J Am Vet Med Assoc [Internet]. 2014 Mar 15 [cited 2021 Feb 10];244(6):699–707. Available from: https://pubmed.ncbi.nlm.nih.gov/24568112/

13.   Malone M, Bjarnsholt T, McBain AJ, James GA, Stoodley P, Leaper D, et al. The prevalence of biofilms in chronic wounds: A systematic review and meta-analysis of published data [Internet]. Vol. 26, Journal of Wound Care. MA Healthcare Ltd; 2017 [cited 2021 Feb 10]. p. 20–5. Available from: https://pubmed.ncbi.nlm.nih.gov/28103163/

14.   Jamal M, Ahmad W, Andleeb S, Jalil F, Imran M, Nawaz MA, et al. Bacterial biofilm and associated infections [Internet]. Vol. 81, Journal of the Chinese Medical Association. Elsevier Ltd; 2018 [cited 2021 Feb 10]. p. 7–11. Available from: https://pubmed.ncbi.nlm.nih.gov/29042186/

15.   Veerachamy S, Yarlagadda T, Manivasagam G, Yarlagadda PK. Bacterial adherence and biofilm formation on medical implants: A review [Internet]. Vol. 228, Proceedings of the Institution of Mechanical Engineers, Part H: Journal of Engineering in Medicine. SAGE Publications Ltd; 2014 [cited 2021 Feb 10]. p. 1083–99. Available from: https://pubmed.ncbi.nlm.nih.gov/25406229/

16.   Rimondini L, Cochis A, Varoni E, Azzimonti B, Carrassi A. Biofilm Formation on Implants and Prosthetic Dental Materials. In: Handbook of Bioceramics and Biocomposites [Internet]. Springer International Publishing; 2015 [cited 2021 Feb

10]. p. 1–37. Available from:
https://link.springer.com/referenceworkentry/10.1007/978-3-319-09230-0_48-1

17. Edmiston CE, McBain AJ, Kiernan M, Leaper DJ. A narrative review of microbial
biofilm in postoperative surgical site infections: Clinical presentation and
treatment [Internet]. Vol. 25, Journal of Wound Care. MA Healthcare Ltd; 2016
[cited 2021 Feb 10]. p. 693–702. Available from:
https://pubmed.ncbi.nlm.nih.gov/27974013/

18. Stoodley P, Sauer K, Davies DG, Costerton JW. Biofilms as Complex
Differentiated Communities. Annu Rev Microbiol [Internet]. 2002 Oct 28 [cited
2021 Apr 2];56(1):187–209. Available from:
http://www.annualreviews.org/doi/10.1146/annurev.micro.56.012302.160705

19. Wan N, Wang H, Ng CK, Mukherjee M, Ren D, Cao B, et al. Bacterial
Metabolism During Biofilm Growth Investigated by 13C Tracing. Front Microbiol
[Internet]. 2018 Nov 20 [cited 2021 Feb 10];9(NOV):2657. Available from:
https://www.frontiersin.org/article/10.3389/fmicb.2018.02657/full

20. Flemming HC, Wingender J. The biofilm matrix [Internet]. Vol. 8, Nature
Reviews Microbiology. Nature Publishing Group; 2010 [cited 2021 Feb 10]. p.
623–33. Available from: https://www.nature.com/articles/nrmicro2415

21. Costerton JW, Stewart PS, Greenberg EP. Bacterial biofilms: A common cause of
persistent infections [Internet]. Vol. 284, Science. Science; 1999 [cited 2021 Feb
10]. p. 1318–22. Available from: https://pubmed.ncbi.nlm.nih.gov/10334980/

22. Bjarnsholt T, Kirketerp-Møller K, Jensen PØ, Madsen KG, Phipps R, Krogfelt K,
et al. Why chronic wounds will not heal: A novel hypothesis [Internet]. Vol. 16,
Wound Repair and Regeneration. Wound Repair Regen; 2008 [cited 2021 Feb 10].
p. 2–10. Available from: https://pubmed.ncbi.nlm.nih.gov/18211573/

23. James GA, Swogger E, Wolcott R, Pulcini ED, Secor P, Sestrich J, et al. Biofilms
in chronic wounds. Wound Repair Regen. 2008;16(1):37–44.

24. Freeman K, Woods E, Welsby S, Percival SL, Cochrane CA. Biofilm evidence and
the microbial diversity of horse wounds. Can J Microbiol [Internet]. 2009 Feb
[cited 2021 Feb 10];55(2):197–202. Available from:

https://pubmed.ncbi.nlm.nih.gov/19295652/

25.   Westgate SJ, Percival SL, Knottenbelt DC, Clegg PD, Cochrane CA. Chronic
        equine wounds: what is the role of infection and biofilms?. Wounds a Compend
        Clin Res Pract [Internet]. 2010 Jun 1 [cited 2021 Feb 10];22(6):138–45. Available
        from: http://www.ncbi.nlm.nih.gov/pubmed/25901461

26.   Futagawa-Saito K, Ba-Thein W, Sakurai N, Fukuyasu T. Prevalence of virulence
        factors in Staphylococcus intermedius isolates from dogs and pigeons. BMC Vet
        Res [Internet]. 2006 Jan 26 [cited 2021 Feb 10];2(1):4. Available from:
        http://bmcvetres.biomedcentral.com/articles/10.1186/1746-6148-2-4

27.   Osland AM, Vestby LK, Fanuelsen H, Slettemeås JS, Sunde M. Clonal diversity
        and biofilm-forming ability of methicillin-resistant Staphylococcus
        pseudintermedius. J Antimicrob Chemother [Internet]. 2012 Apr [cited 2021 Feb
        10];67(4):841–8. Available from: https://pubmed.ncbi.nlm.nih.gov/22258925/

28.   Damborg P, Moodley A, Aalbæk B, Ventrella G, dos Santos TP, Guardabassi L.
        High genotypic diversity among methicillin-resistant Staphylococcus
        pseudintermedius isolated from canine infections in Denmark. BMC Vet Res
        [Internet]. 2016 Jun 29 [cited 2021 Feb 10];12(1). Available from:
        https://pubmed.ncbi.nlm.nih.gov/27357502/

29.   Saab ME, Weese JS, McClure JT. Direct repeat unit (dru) typing and antimicrobial
        resistance of methicillin-resistant staphylococcus pseudintermedius isolated from
        dogs in atlantic Canada. Can J Vet Res [Internet]. 2017 [cited 2021 Feb
        10];81(3):192–8. Available from: www.dru-typing.org

30.   Corrò M, Skarin J, Börjesson S, Rota A. Occurrence and characterization of
        methicillin-resistant Staphylococcus pseudintermedius in successive parturitions of
        bitches and their puppies in two kennels in Italy. BMC Vet Res [Internet]. 2018
        Dec 11 [cited 2021 Feb 10];14(1):308. Available from:
        https://bmcvetres.biomedcentral.com/articles/10.1186/s12917-018-1612-z

31.   Wolcott R, Costerton JW, Raoult D, Cutler SJ. The polymicrobial nature of
        biofilm infection. Vol. 19, Clinical Microbiology and Infection. Blackwell
        Publishing Ltd; 2013. p. 107–12.

32. Attinger C, Wolcott R. Clinically Addressing Biofilm in Chronic Wounds. Adv Wound Care [Internet]. 2012 Jun [cited 2021 Feb 10];1(3):127–32. Available from: /pmc/articles/PMC3839004/

33. Gordillo GM, Bernatchez SF, Diegelmann R, Di Pietro LA, Eriksson E, Hinz B, et al. Preclinical Models of Wound Healing: Is Man the Model? Proceedings of the Wound Healing Society Symposium. Adv Wound Care [Internet]. 2013 Feb [cited 2021 Feb 10];2(1):1–4. Available from: /pmc/articles/PMC3840478/

34. Wolcott RD, Kennedy JP, Dowd SE. Regular debridement is the main tool for maintaining a healthy wound bed in most chronic wounds. [Internet]. Vol. 18, Journal of wound care. J Wound Care; 2009 [cited 2021 Feb 10]. p. 54–6. Available from: https://pubmed.ncbi.nlm.nih.gov/19418781/

35. Percival SL, McCarty SM, Lipsky B. Biofilms and Wounds: An Overview of the Evidence. Adv Wound Care [Internet]. 2015 Jul [cited 2021 Feb 10];4(7):373–81. Available from: /pmc/articles/PMC4486148/

36. Rowan MP, Cancio LC, Elster EA, Burmeister DM, Rose LF, Natesan S, et al. Burn wound healing and treatment: Review and advancements [Internet]. Vol. 19, Critical Care. BioMed Central Ltd.; 2015 [cited 2021 Feb 10]. Available from: /pmc/articles/PMC4464872/

37. Wolcott RD, Rhoads DD, Dowd SE. Biofilms and chronic wound inflammation. [Internet]. Vol. 17, Journal of wound care. J Wound Care; 2008 [cited 2021 Feb 10]. p. 333–41. Available from: https://pubmed.ncbi.nlm.nih.gov/18754194/

38. Granick M, Boykin J, Gamelli R, Schultz G, Tenenhaus M. Toward a common language: surgical wound bed preparation and debridement. Wound Repair Regen [Internet]. 2006 May [cited 2021 Feb 10];14(s1):S1–10. Available from: http://doi.wiley.com/10.1111/j.1524-475X.2005.00096.x

39. Namgoong S, Jung SY, Han SK, Kim AR, Dhong ES. Clinical experience with surgical debridement and simultaneous meshed skin grafts in treating biofilm-associated infection: an exploratory retrospective pilot study. J Plast Surg Hand Surg [Internet]. 2020 Jan 2 [cited 2021 Feb 10];54(1):47–54. Available from: https://pubmed.ncbi.nlm.nih.gov/31575315/

40. Clinton A, Carter T. Chronic wound biofilms: Pathogenesis and potential therapies [Internet]. Vol. 46, Lab Medicine. Oxford University Press; 2015 [cited 2021 Feb 10]. p. 277–84. Available from: https://pubmed.ncbi.nlm.nih.gov/26489671/

41. Cooper RA, Bjarnsholt T, Alhede M. Biofilms in wounds: A review of present knowledge. J Wound Care [Internet]. 2014 Nov 1 [cited 2021 Feb 10];23(11):570–82. Available from: https://pubmed.ncbi.nlm.nih.gov/25375405/

42. Jones CE, Kennedy JP. Treatment Options to Manage Wound Biofilm.

43. Wolcott RD, Rumbaugh KP, James G, Schultz G, Phillips P, Yang Q, et al. Biofilm maturity studies indicate sharp debridement opens a timedependent therapeutic window. J Wound Care [Internet]. 2010 [cited 2021 Feb 10];19(8):320–8. Available from: https://pubmed.ncbi.nlm.nih.gov/20852503/

44. Tahir S, Malone M, Hu H, Deva A, Vickery K. The effect of negative pressurewound therapy with and without instillation on mature biofilms in vitro. Materials (Basel) [Internet]. 2018 May 16 [cited 2021 Feb 10];11(5). Available from: https://pubmed.ncbi.nlm.nih.gov/29772696/

45. Koob TJ, Lim JJ, Massee M, Zabek N, Denozière G. Properties of dehydrated human amnion/chorion composite grafts: Implications for wound repair and soft tissue regeneration. J Biomed Mater Res - Part B Appl Biomater [Internet]. 2014 [cited 2021 Mar 24];102(6):1353–62. Available from: https://pubmed.ncbi.nlm.nih.gov/24664953/

46. Matica MA, Lillelund Aachmann F, Tøndervik A, Sletta H, Ostafe V. Molecular Sciences Chitosan as a Wound Dressing Starting Material: Antimicrobial Properties and Mode of Action. [cited 2021 Mar 24]; Available from: www.mdpi.com/journal/ijms

47. Brett D. A Review of Collagen and Collagen-based Wound Dressings. Wounds [Internet]. 2008 [cited 2021 Mar 24];20(12). Available from: https://www.woundsresearch.com/content/a-review-collagen-and-collagen-based-wound-dressings

48. Mandla S, Davenport Huyer L, Radisic M. Review: Multimodal bioactive material approaches for wound healing. 2013 [cited 2021 Apr 12]; Available from:

https://doi.org/10.1063/1.5026773

49. Madhumathi K, Sudheesh Kumar PT, Abhilash S, Sreeja V, Tamura H, Manzoor K, et al. Development of novel chitin/nanosilver composite scaffolds for wound dressing applications. J Mater Sci Mater Med [Internet]. 2010 Feb [cited 2021 Apr 12];21(2):807–13. Available from: https://pubmed.ncbi.nlm.nih.gov/19802687/

50. van Loosdrecht MCM, Lyklema J, Norde W, Zehnder AJB. Bacterial adhesion: A physicochemical approach. Microb Ecol [Internet]. 1989 Jan [cited 2021 Feb 10];17(1):1–15. Available from: https://link.springer.com/article/10.1007/BF02025589

51. Blenkinsopp SA, Khoury AE, Costerton JW. Electrical enhancement of biocide efficacy against Pseudomonas aeruginosa biofilms [Internet]. Vol. 58, Applied and Environmental Microbiology. American Society for Microbiology (ASM); 1992 [cited 2021 Feb 10]. p. 3770–3. Available from: /pmc/articles/PMC183173/?report=abstract

52. Barker AT, Jaffe LF, Vanable JW. The glabrous epidermis of cavies contains a powerful battery. Am J Physiol - Regul Integr Comp Physiol [Internet]. 1982 [cited 2021 Feb 10];11(2). Available from: https://journals.physiology.org/doi/abs/10.1152/ajpregu.1982.242.3.R358

53. FOULDS IS, BARKER AT. Human skin battery potentials and their possible role in wound healing. Br J Dermatol [Internet]. 1983 [cited 2021 Feb 10];109(5):515–22. Available from: https://pubmed.ncbi.nlm.nih.gov/6639877/

54. Zhao M. Electrical fields in wound healing-An overriding signal that directs cell migration. Vol. 20, Seminars in Cell and Developmental Biology. Elsevier Ltd; 2009. p. 674–82.

55. Nuccitelli R, Nuccitelli P, Li C, Narsing S, Pariser DM, Lui K. The electric field near human skin wounds declines with age and provides a noninvasive indicator of wound healing. Wound Repair Regen [Internet]. 2011 Sep [cited 2021 Feb 10];19(5):645–55. Available from: /pmc/articles/PMC3228273/

56. Nuccitelli R. Endogenous ionic currents and DC electric fields in multicellular animal tissues. Bioelectromagnetics [Internet]. 1992 [cited 2021 Feb 10];13(1

S):147–57. Available from: https://pubmed.ncbi.nlm.nih.gov/1285710/

57.   Zhao M. Electrical fields in wound healing-An overriding signal that directs cell migration [Internet]. Vol. 20, Seminars in Cell and Developmental Biology. Elsevier Ltd; 2009 [cited 2021 Feb 10]. p. 674–82. Available from: https://pubmed.ncbi.nlm.nih.gov/19146969/

58.   Reid B, Nuccitelli R, Zhao M. Non-invasive measurement of bioelectric currents with a vibrating probe. Nat Protoc. 2007 Mar 29;2(3):661–9.

59.   Nishimura KY, Isseroff RR, Nuccitelli R. Human keratinocytes migrate to the negative pole in direct current electric fields comparable to those measured in mammalian wounds. J Cell Sci. 1996;109:199–207.

60.   Sebastian A, Iqbal SA, Colthurst J, Volk SW, Bayat A. Electrical Stimulation Enhances Epidermal Proliferation in Human Cutaneous Wounds by Modulating p53-SIVA1 Interaction. J Invest Dermatol. 2015 Apr 20;135(4):1166–74.

61.   Hoare JI, Rajnicek AM, McCaig CD, Barker RN, Wilson HM. Electric fields are novel determinants of human macrophage functions. J Leukoc Biol [Internet]. 2016 Jun 1 [cited 2021 Mar 24];99(6):1141–51. Available from: http://doi.wiley.com/10.1189/jlb.3A0815-390R

62.   Guo A, Song B, Reid B, Gu Y, Forrester J V., Jahoda CAB, et al. Effects of physiological electric fields on migration of human dermal fibroblasts. J Invest Dermatol. 2010;130(9):2320–7.

63.   Ud-Din S, Sebastian A, Giddings P, Colthurst J, Whiteside S, Morris J, et al. Angiogenesis is induced and wound size is reduced by electrical stimulation in an acute wound healing model in human skin. PLoS One [Internet]. 2015 Apr 30 [cited 2021 Feb 5];10(4). Available from: /pmc/articles/PMC4415761/?report=abstract

64.   Banerjee J, Das Ghatak P, Roy S, Khanna S, Sequin EK, Bellman K, et al. Improvement of human keratinocyte migration by a redox active bioelectric dressing. PLoS One. 2014;9(3).

65. Bogie KM. The Modular Adaptive Electrotherapy Delivery System (MAEDS): An Electroceutical Approach for Effective Treatment of Wound Infection and Promotion of Healing. Mil Med [Internet]. 2019 Mar 1 [cited 2021 Apr 12];184(Supplement_1):92–6. Available from: https://academic.oup.com/milmed/article/184/Supplement_1/92/5160928

66. Howe DS, Dunning J, Zorman C, Garverick SL, Bogie KM. Development of an Integrated Surface Stimulation Device for Systematic Evaluation of Wound Electrotherapy. Ann Biomed Eng [Internet]. 2015 Feb 1 [cited 2021 Apr 12];43(2):306–13. Available from: https://link.springer.com/article/10.1007/s10439-014-1134-1

67. Kambouris ME, Markogiannakis A, Arabatzis M, Manoussopoulos Y, Kantzanou M, Velegraki A. Wireless electrostimulation: A new approach in combating infection? [Internet]. Vol. 12, Future Microbiology. Future Medicine Ltd.; 2017 [cited 2021 Feb 10]. p. 255–65. Available from: https://pubmed.ncbi.nlm.nih.gov/28262048/

68. Sandvik EL, McLeod BR, Parker AE, Stewart PS. Direct Electric Current Treatment under Physiologic Saline Conditions Kills Staphylococcus epidermidis Biofilms via Electrolytic Generation of Hypochlorous Acid. Otto M, editor. PLoS One [Internet]. 2013 Feb 4 [cited 2021 Feb 10];8(2):e55118. Available from: https://dx.plos.org/10.1371/journal.pone.0055118

69. Heald R, Bennett M, Subramaniam V V., Dusane D, Lochab V, Sundaram PM, et al. Printed Electroceutical Dressings for the Inhibition of Biofilms and Treatment of Chronic Wounds. J Microelectromechanical Syst. 2020 Oct 1;29(5):918–23.

70. Sultana ST, Atci E, Babauta JT, Mohamed Falghoush A, Snekvik KR, Call DR, et al. Electrochemical scaffold generates localized, low concentration of hydrogen peroxide that inhibits bacterial pathogens and biofilms. Sci Rep [Internet]. 2015 Oct 14 [cited 2021 Feb 18];5:14908–14908. Available from: www.nature.com/scientificreports

71. Roy S, Prakash S, Mathew-Steiner SS, Das Ghatak P, Lochab V, Jones TH, et al. Disposable Patterned Electroceutical Dressing (PED-10) Is Safe for Treatment of Open Clinical Chronic Wounds. Adv Wound Care. 2019;8(4):149–59.

72. Chang W, Small DA, Toghrol F, Bentley WE. Global transcriptome analysis of

Staphylococcus aureus response to hydrogen peroxide. J Bacteriol [Internet]. 2006 [cited 2021 Feb 18];188(4):1648–59. Available from: /pmc/articles/PMC1367260/

73. Leonel C, Sena IFG, Silva WN, Prazeres PHDM, Fernandes GR, Mancha Agresti P, et al. Staphylococcus epidermidis role in the skin microenvironment. J Cell Mol Med [Internet]. 2019 [cited 2021 Feb 18];23(9):5949–55. Available from: /pmc/articles/PMC6714221/

74. Wilson APR, Grüneberg RN, Treasure T, Sturridge MF. Staphylococcus epidermidis as a cause of postoperative wound infection after cardiac surgery: Assessment of pathogenicity by a wound-scoring method. Br J Surg [Internet]. 1988 Feb 1 [cited 2021 Feb 18];75(2):168–70. Available from: http://doi.wiley.com/10.1002/bjs.1800750228

75. Giacometti A, Cirioni O, Schimizzi AM, Del Prete MS, Barchiesi F, D'Errico MM, et al. Epidemiology and microbiology of surgical wound infections. J Clin Microbiol [Internet]. 2000 [cited 2021 Feb 18];38(2):918–22. Available from: https://pubmed.ncbi.nlm.nih.gov/10655417/

76. Schierle CF, De La Garza M, Mustoe TA, Galiano RD. Staphylococcal biofilms impair wound healing by delaying reepithelialization in a murine cutaneous wound model. Wound Repair Regen [Internet]. 2009 [cited 2021 Feb 18];17(3):354–9. Available from: https://pubmed.ncbi.nlm.nih.gov/19660043/

77. Dusane DH, Lochab V, Jones T, Peters CW, Sindeldecker D, Das A, et al. Electroceutical Treatment of Pseudomonas aeruginosa Biofilms. Sci Rep [Internet]. 2019;9(1):1–13. Available from: http://dx.doi.org/10.1038/s41598-018-37891-y

78. Guo A, Song B, Reid B, Gu Y, Forrester J V., Jahoda CAB, et al. Effects of physiological electric fields on migration of human dermal fibroblasts. J Invest Dermatol [Internet]. 2010 Sep 1 [cited 2021 Mar 24];130(9):2320–7. Available from: www.jidonline.org

79. Chen JS, Longaker MT, Gurtner GC. Murine models of human wound healing. Methods Mol Biol [Internet]. 2013 [cited 2021 Feb 18];1037:265–74. Available from: /pmc/articles/PMC5839669/

80. Galiano RD, Michaels, V J, Dobryansky M, Levine JP, Gurtner GC. Quantitative and reproducible murine model of excisional wound healing. Wound Repair Regen [Internet]. 2004 Aug 1 [cited 2021 Mar 17];12(4):485–92. Available from: http://doi.wiley.com/10.1111/j.1067-1927.2004.12404.x

81. Miklavĉiĉ D, Vodovnik L, Bobanovic F, Reberŝek S, Serŝa G, Novaković S, et al. Local treatment of murine tumors by electric direct Current. Electromagn Biol Med [Internet]. 1992 [cited 2021 Mar 23];11(2):109–25. Available from: https://www.tandfonline.com/doi/abs/10.3109/15368379209009821

82. Bryan J. Moist wound healing: a concept that changed our practice. [Internet]. Vol. 13, Journal of wound care. MA Healthcare London ; 2004 [cited 2021 Feb 21]. p. 227–8. Available from: https://www.magonlinelibrary.com/doi/abs/10.12968/jowc.2004.13.6.26625

83. Winter GD. Effect of air exposure and occlusion on experimental human skin wounds [32] [Internet]. Vol. 200, Nature. Nature Publishing Group; 1963 [cited 2021 Feb 21]. p. 378–9. Available from: https://www.nature.com/articles/200378a0

84. Ewing SG, Lipski WJ, Grace AA, Winter C. An inexpensive, charge-balanced rodent deep brain stimulation device: A step-by-step guide to its procurement and construction. J Neurosci Methods. 2013 Oct 15;219(2):324–30.

85. Leal C, Lopes PA, Serra AA, Coelho JFJ, De Almeida AT, Tavakoli M. Untethered Disposable Health Monitoring Electronic Patches with an Integrated Ag 2 O−Zn Battery, a AgInGa Current Collector, and Hydrogel Electrodes. Cite This ACS Appl Mater Interfaces [Internet]. 2020 [cited 2021 Feb 4];12:3407–14. Available from: https://dx.doi.org/10.1021/acsami.9b18462

86. Li Y, Yong S, Hillier N, Arumugam S, Beeby S. Screen Printed Flexible Water Activated Battery on Woven Cotton Textile as a Power Supply for E-Textile Applications. IEEE Access. 2020;8:206958–65.

87. Braam KT, Volkman SK, Subramanian V. Characterization and optimization of a printed, primary silver-zinc battery. J Power Sources. 2012;199:367–72.

88. Vilkhu R, Thio WJC, Das Ghatak P, Sen CK, Co AC, Kiourti A. Power

Generation for Wearable Electronics: Designing Electrochemical Storage on Fabrics. IEEE Access. 2018;6:28945–50.

89.   Nguyen TH, Fraiwan A, Choi S. Paper-based batteries: A review. 2013 [cited 2021 Feb 4]; Available from: http://dx.doi.org/10.1016/j.bios.2013.11.007

90.   Cheng Q, Song Z, Ma T, Smith BB, Tang R, Yu H, et al. Folding Paper-Based Lithium-Ion Batteries for Higher Areal Energy Densities. 2021 [cited 2021 Feb 4];4:23. Available from: https://pubs.acs.org/sharingguidelines

91.   Sousa RE, Costa CM, Lanceros-Méndez S. Advances and Future Challenges in Printed Batteries. ChemSusChem. 2015 Nov 1;8(21):3539–55.

92.   Tavakoli M, Rocha R, Osorio L, Almeida M, De Almeida A, Ramachandran V, et al. Carbon doped PDMS: Conductance stability over time and implications for additive manufacturing of stretchable electronics. J Micromechanics Microengineering. 2017;27(3).

93.   Tavakoli M, Malakooti MH, Paisana H, Ohm Y, Green Marques D, Alhais Lopes P, et al. EGaIn-Assisted Room-Temperature Sintering of Silver Nanoparticles for Stretchable, Inkjet-Printed, Thin-Film Electronics. Adv Mater. 2018 Jul 19;30(29).

94.   Gu M, Song WJ, Hong J, Kim SY, Shin TJ, Kotov NA, et al. Stretchable batteries with gradient multilayer conductors. Sci Adv [Internet]. 2019 Jul 26 [cited 2021 Feb 4];5(7):eaaw1879. Available from: http://advances.sciencemag.org/

95.   Karpinski AP, Makovetski B, Russell SJ, Serenyi JR, Williams DC. Silver-zinc: status of technology and applications. Vol. 80, Journal of Power Sources.

96.   Mauger A, Julien CM. Critical review on lithium-ion batteries: are they safe? Sustainable? [Internet]. Vol. 23, Ionics. Institute for Ionics; 2017 [cited 2021 Feb 4]. p. 1933–47. Available from: https://www.ev-power.eu/LTO-Cells/

97.   Li C, Zhang Q, Sun J, Li T, Zhu Z, He B, et al. High-Performance Quasi-Solid-State Flexible Aqueous Rechargeable Ag−Zn Battery Based on Metal−Organic Framework-Derived Ag Nanowires. ACS Energy Lett [Internet]. 2018 [cited 2021 Feb 4];3. Available from: http://pubs.acs.org/journal/aelccp

98. Miguel Esperanc D, Sofia Taborda Martins Pereira A, Carranca Almeida nio, Santana Roma U, Ben Aissa Soler A, Lacharmoise PD, et al. Large-Area Paper Batteries with Ag and Zn/Ag Screen-Printed Electrodes. 2019 [cited 2021 Feb 4]; Available from: https://pubs.acs.org/sharingguidelines

99. Kumar R, Shin J, Yin L, You JM, Meng YS, Wang J. All-Printed, Stretchable Zn-Ag2O Rechargeable Battery via Hyperelastic Binder for Self-Powering Wearable Electronics. Adv Energy Mater. 2017 Apr 19;7(8).

100. Winter M, Brodd RJ. What are batteries, fuel cells, and supercapacitors? Chem Rev [Internet]. 2004 Oct [cited 2021 Mar 1];104(10):4245–69. Available from: https://pubs.acs.org/sharingguidelines

101. Elgrishi N, Rountree KJ, McCarthy BD, Rountree ES, Eisenhart TT, Dempsey JL. A Practical Beginner's Guide to Cyclic Voltammetry. J Chem Educ [Internet]. 2018 Feb 13 [cited 2021 Feb 18];95(2):197–206. Available from: https://pubs.acs.org/sharingguidelines

102. Morehouse CK, Glicksman R, Lozier GS. Batteries. Proc IRE. 1958;46(8):1462–83.

103. GD M. Quantifying wound fluids for the clinician and researcher. Ostomy Wound Manag. 1994;40(8):66–9.

104. Kiamco MM, Zmuda HM, Mohamed A, Call DR, Raval YS, Patel R, et al. Hypochlorous-Acid-Generating Electrochemical Scaffold for Treatment of Wound Biofilms. Sci Rep [Internet]. 2019 Dec 1 [cited 2021 Feb 18];9(1):1–13. Available from: https://doi.org/10.1038/s41598-019-38968-y

105. McAdams E. Bioelectrodes. In: Encyclopedia of Medical Devices and Instrumentation [Internet]. Hoboken, NJ, USA: John Wiley & Sons, Inc.; 2006 [cited 2021 Apr 13]. Available from: http://doi.wiley.com/10.1002/0471732877.emd013

106. Rosell J, Colominas J, Riu P, Pallas-Areny R, Webster JG. Skin Impedance From 1 Hz to 1 MHz. IEEE Trans Biomed Eng. 1988;35(8):649–52.

107. Eming SA, Martin P, Tomic-Canic M. Wound repair and regeneration: Mechanisms, signaling, and translation. Sci Transl Med. 2014;6(265).

Table 6. The wound area measurements for the four mice in Group T1 with the 5.6 µA PED on the right-side wound and the silk covering on the left-side wound.

Group A	Wound area (mm²): PED, 5.6 µA				Wound area (mm²): Silk covering			
	Day 0	Day 2	Day 4	Day 7	Day 0	Day 2	Day 4	Day 7
Mouse 1	25.1	20.8	7.8	0.1	17.0	18.3	10.8	2.7
Mouse 2	26.5	19.0	8.8	0.2	17.6	16.4	9.0	0.2
Mouse 3	36.8	22.7	11.9	0.2	36.0	32.9	18.0	5.8
Mouse 4	32.4	21.0	11.9	0.5	30.1	23.6	15.6	11.1

Table 5. The percent decrease in wound area from Day 0 for Group T1 wounds. The gray shaded cells indicate that the dressing came off the mouse 24 hours prior.

Group A	Wound 1: 270 kΩ PED, 5.6 µA			Wound 2: Silk covering		
	Day 2	Day 4	Day 7	Day 2	Day 4	Day 7
Mouse 1	17.3%	69.0%	99.6%	-7.8%	36.4%	87.3%
Mouse 2	28.4%	66.7%	99.3%	6.7%	48.9%	99.0%
Mouse 3	39.8%	67.7%	99.5%	8.8%	50.0%	84.0%
Mouse 4	35.2%	63.4%	98.5%	21.6%	48.3%	63.1%
Average	30.2%	66.7%	99.2%	7.3%	45.9%	83.3%

Table 7. The wound area measurements for the four mice in Group T2 with the 56 μA PED on the right-side wound and the silk covering on the left-side wound.

Group B	Wound area (mm²): PED, 56 μA				Wound area (mm²): Silk covering			
	Day 0	Day 2	Day 4	Day 7	Day 0	Day 2	Day 4	Day 7
Mouse 1	26.7	25.7	6.5	0.4	35.3	39.8	26.4	12.2
Mouse 2	41.1	28.7	14.5	0.7	38.7	29.9	12.5	0.2
Mouse 3	27.6	22.0	10.1	0.8	21.6	25.4	18.2	3.7
Mouse 4	25.8	15.9	8.8	0.5	28.9	35.4	18.5	4.1

Table 8. The percent decrease in wound area from Day 0 for Group T2 wounds. The gray shaded cells indicate that the dressing came off the mouse 24 hours prior. Negative percentages indicate when the wound area increased in size compared to Day 0.

Group B	Wound 1: 27 kΩ PED, 56 μA			Wound 2: Silk covering		
	Day 2	Day 4	Day 7	Day 2	Day 4	Day 7
Mouse 1	3.7%	75.7%	98.3%	-12.9%	25.2%	65.4%
Mouse 2	30.2%	64.8%	98.2%	22.6%	67.6%	99.5%
Mouse 3	20.1%	63.5%	97.2%	-17.9%	15.4%	82.8%
Mouse 4	38.3%	65.9%	98.2%	-22.6%	36.0%	85.9%
Average	23.1%	67.5%	98.0%	-7.7%	36.0%	83.4%

Table 10. The wound area measurements for the four mice in Group C with the electrodes only on the right-side wound and the silk covering on the left-side wound.

Group C	Wound area (mm²): Electrodes only				Wound area (mm²): Silk covering			
	Day 0	Day 2	Day 4	Day 7	Day 0	Day 2	Day 4	Day 7
Mouse 1	25.3	7.7	10.2	0.9	28.8	17.3	16.7	10.9
Mouse 2	25.0	10.9	3.4	0.5	22.1	21.5	16.3	6.0
Mouse 3	23.4	5.9	7.1	0	41.7	27.2	24.4	7.5
Mouse 4	29.9	9.6	4.6	0.4	24.7	18.1	16.3	10.5

Table 9. The percent decrease in wound area from Day 0 for Group C wounds. The gray shaded cells indicate that the dressing came off the mouse 24 hours prior.

Group C	Wound 1: Electrodes only			Wound 2: Silk covering		
	Day 2	Day 4	Day 7	Day 2	Day 4	Day 7
Mouse 1	69.4%	59.5%	96.6%	39.9%	42.1%	62.2%
Mouse 2	56.5%	86.6%	98.2%	2.7%	26.3%	73.0%
Mouse 3	75.0%	69.5%	100%	34.9%	41.6%	82.0%
Mouse 4	68.0%	84.7%	98.8%	26.6%	33.9%	57.7%
Average	67.2%	75.1%	98.4%	26.0%	36.0%	68.7%

Appendix B: Flexible Battery Cells in Series

Table 11. Ag/AgCl-Zn cells were placed in series by conductive thread and epoxy, wetted with 1X PBS and the open circuit voltage was measured. The open circuit voltage scaling nearly linearly, with each cell adding ~0.67V.

Number of cells in series	Open circuit (V)
1	0.81 ± 0.04
2	1.52 ± 0.05
3	2.12 ± 0.07
4	2.70 ± 0.07
5	3.21 ± 0.01
6	3.83 ± 0.10
7	4.69 ± 0.02
8	5.49 ± 0.06
9	6.27 ± 0.04

Appendix C: Process Documents

C.1 PED Fabrication

Screen Printing PED Electrodes

Note: This process has been updated from Molly Bennett's thesis, *Design, Fabrication, and Characterization of Electroceutical Bandages for Treatment of Chronically Infected Wounds*

Materials:
- Masking tape
- Hot plate
- Pencil
- Jacquard Ink Jet Printable Silk
- Fabric Scissoring
- 18" x 20" wood frame screen with developed pattern and attached to base
- Fisher Scientific BD 1 mL Slip Tip syringe
- Screen Grafex Easy Grip 70 Duro Wood Handle Yellow
- Silver/Silver Chloride Ink (Creative Materials #113-09)
- Ink Thinner (Creative Materials #102-03)

Procedure:
1. Place hot plate in a fume hood to prevent inhalation of fumes while ink cures.
2. Preheat the hot plate to 125°C.
3. Measure and mark guidelines on the paper side of the printable silk with a pencil. Size of silk strips is dependent on the desired design to print. The strips should be measured and cut to allow for at least 0.25" clearance on all sides of the printed design. For the designs used in this Master's thesis, silk strips were cut to around 3.5" by 8.5" to obtain 3 bandages per sheet of silk paper.

78

4. Cut out 10 to 15 pre-measured strips of printable silk using sharp fabric scissors. This printing method can yield about 10-15 printed bandages before the ink begins to harden in the screen mesh, restricting ink from transferring to the fabric.

5. Measure and mark the parchment paper on the screen base to assist in alignment of the printable silk before each print. Before any ink is spread across the screen, the screen remains partially transparent, and alignment can be checked through the screen. Once the proper alignment is achieved, mark the locations of the corners of the silk strip on the parchment paper in pen or pencil. The edges of the silk strip should be approximately parallel to the pattern, however excess fabric will be trimmed in the final stages of fabrication.

6. Place the screen and base board assembly in the fume hood.

7. Collect and place the following supplies in the hood on a paper towel next to the screen assembly:
   a. Fisher Scientific BD 1 mL Slip Tip syringe (2)
   b. Ag/AgCl ink
   c. Ink thinner
   d. Squeegee

8. Align a strip of printable silk to the guidelines drawn on the screen base board.

9. Tape the bottom and top edges of the printable silk strip to the lined screen base board using masking tape. Only overlap enough of the silk strip to keep it in place during printing to minimize the fraying upon removal. Also check to make sure the tape does not block any of the pattern before printing. Lower screen onto baseboard to begin printing.

10. Stir the Ag/AgCl ink with the slip tip syringe to resuspend silver particles.

11. Obtain 0.5 mL of Ag/AgCl ink in slip tip syringe.

12. Deposit ink onto screen, distributing among the top edges of the pattern.

13. Contact the edge of the squeegee to the screen above the deposited ink. Draw the squeegee through the ink and across the entire pattern using uniform pressure and moving at a constant speed. The first pass of ink deposition has now been

completed. The first bandage printed in any given session will require an extra pass to fill the screen with ink. All subsequent bandages in the printing session should require 2-3 passes with ink.

14. Scrape excess ink from the squeegee back into the ink container using a plastic spatula.

15. Draw the squeegee over the pattern without ink to transfer ink from the screen to the silk. After every pass completed using ink, a pass without ink is performed as well.

16. Repeat passes with and without ink until pattern appears uniform (2-3 passes with ink). Check pattern after 2 passes by lifting screen and optically examining pattern for uniformity. Remember, the first bandage printed in a session will require an additional pass compared to subsequent bandages.

17. Carefully remove masking tape from printable silk without smudging pattern of fraying silk. Hole the silk stationary with one hand and slowly peel the tape off with the other.

18. Carefully peel the silk pattern from the paper backing without stretching the silk or smudging/distorting the pattern.

19. Place the printed silk on the preheated hot plate with the pattern facing upward.

20. Allow the ink to cure for 10-12 minutes depending on the area of pattern and amount of ink. Ink will lighten in color and appear shiny as it cures. Curing allows the suspended silver particles to sinter together and form a more uniform pattern.

21. Remove cured silk from hot plate and weigh down as it cools to minimize curling and deformation of the pattern.

22. .Repeat steps 8-21 until desired number of bandages are printed and cured.

23. Use clean room paper towels, slip tip syringe, and 102-03 thinner to clean up all ink from screen and squeegee. Dispose of waste in the EHS solid waste bin after ink dries.

Adherence of Commercial Battery Pack with Conductive Epoxy

Note: This process has been modified from Molly Bennett's thesis, *Design, Fabrication, and Characterization of Electroceutical Bandages for Treatment of Chronically Infected Wounds*

Materials:

- Masking tape
- Hot plate
- CircuitWorks Silver Conductive Epoxy Part A and B
- Small Fisher Scientific BD weigh dish with lid
- Pyrex Petri dish
- Scale
- Toothpick
- 6 V commercial battery pack (Conwork CR2032 Spring Clip Coin Battery Holder Case with ON-OFF Switch)
- Wire cutters
- Tweezers
- Printed electrodes on silk substrates

Procedure:

1. Preheat the hot plate to 80°C.
2. Collect the following tools for epoxy application and place on clean room towel:
   a. CircuitWorks Two-Part Epoxy
   b. Fisher Scientific weigh dish
   c. Toothpick
3. Weigh dish base on scale and tare scale.
4. Slowly deposit desired amount of Part A epoxy in dish on the scale. (Note: ~1 g needed for 5 bandages or 10 wire attachments).
5. Record the mass of Part A and tare scale.

6. Slowly deposit an equal mass of Part B epoxy in the dish on the scale. (Note: Part B is denser than Part A, so a smaller volume of Part B is required to achieve the same mass).

7. Use toothpick to mix the two components together in the dish for about 1 minute.

8. Strip the last 0.5" of each wire on the ON-OFF switch battery pack to be connected.

9. Align the stripped wires so they overlap the lead pads of the electrodes and lightly adhere the excess wire to silk beyond lead pad with tape.

10. Use the toothpick to deposit a bead of silver epoxy over the lead wire onto the lead pad.

11. Carefully place leads on hot plate with electrode supported off to the side.

12. After 1 minute of curing, gently remove the tape with tweezers. Be careful not to disturb the lead embedded in epoxy.

13. Cover the leads a propped glass Pyrex Petri dish to create an oven over the leads and help the epoxy cure more uniformly.

14. Allow the epoxy to cure for 10 minutes at 80°C.

15. Remove Petri dish and silk with pattern and attached leads from hot plate.

Sealing Circuit Connections and Backing the Electrodes with Medical Tape

Note: This process has been modified from Molly Bennett's thesis, *Design, Fabrication, and Characterization of Electroceutical Bandages for Treatment of Chronically Infected Wounds*

Materials:

- Waterproof Medical Tape (BAND-AID® Water Block Tape)
- Fabric scissors
- Screen-printed dressings with epoxied commercial battery pack

Procedure:

1. Cut out strips of medical tape to adhere to the screen-printed side of the pattern on the silk, across the width of the pattern. Overlap the printed pattern by at least 0.25" on either side and at the bottom. Smooth the tape against the silk and pattern to ensure good adhesion.

2. Place another strip of medical tape on the dressing over the electrodes slightly overlapping the previous piece. Again, smooth the tape against the silk and pattern. Repeat until the 7.5 cm x 7.5 cm block of interdigitated electrode are covered.

3. Fold the elongated part of the electrodes that are not covered by medical tape back so that they lay along the medical tape side of the 7.5 cm x 7.5 cm block.

4. Repeating the medical tape layering process as in step 1 and 2, cover the remainder of the electrodes. The epoxied connection between the commercial battery pack and the electrodes should also be covered with medical tape.

5. If needed, keep folding the electrodes back onto the original 7.5 cm x 7.5 cm block and sealing each layer with medical tape until both electrodes and circuit connections are fully concealed (Figure 31).
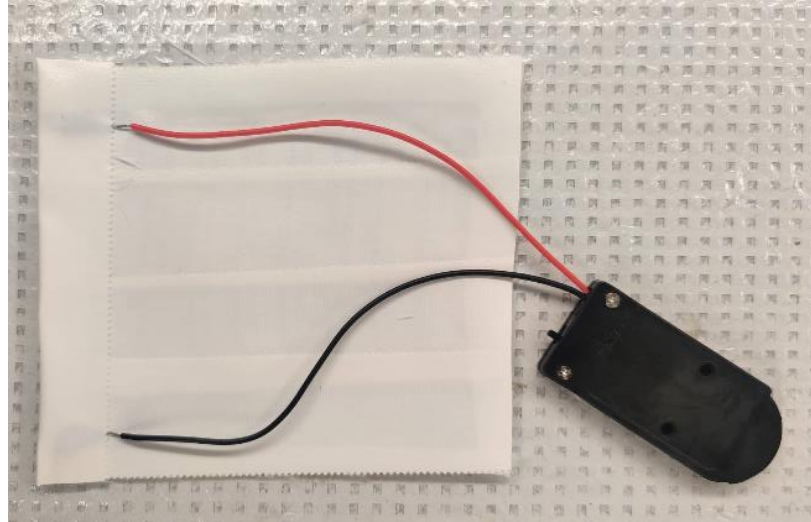
Figure 31. The medical tape concealing the electrodes folded back on themselves. The circuit connections are also concealed by medical tape, exposing the commercial battery pack.

6. Store the finished bandages in ziplock bags to protect bandages and minimize

   contamination.

C.2 Flexible Battery Fabrication

Zinc Ink

Materials:

- Polyvinyl alcohol (PVA)
- Zinc dust (<10 μm)
- Dimethyl sulfoxide (DMSO)
- Glass beaker (150 mL)
- Hot plate
- Stir bar

Procedure:

1. Preheat the hot plate to 80°C.
2. Put 7 mL of DMSO into a glass beaker and place it on the hot plate. Place the stir bar into the beaker and turn it to ~100 rpm.
3. In separate containers, measure out 1 gram of PVA and 4 grams of Zn.
4. Slowly add the PVA to the beaker at 0.5 g/min.
5. Let the PVA mix into the DMSO until dissociated (~30 min).
6. Slowly add the Zn to the beaker at 0.5 g/min.
7. Let the mixture stir for an additional 5 minutes before use.
8. Use the zinc ink immediately.

Screen Printing Ag/AgCl-Zn Cells

Materials:

- Masking tape
- Hot plate
- Jacquard Ink-Jet Printable Silk (Blick Art Materials #64929-1003)
- Fabric/Non-stick Scissors
- Screen with developed pattern and base
- Fisher Scientific BD 1 mL Slip Tip syringe
- Screen Grafex Easy Grip 70 Duro Wood Handle Yellow
- Silver/Silver Chloride Ink (Creative Materials #113-09)
- Ink Thinner (Creative Materials #102-03)
- In-house zinc ink
- Glass beaker (250 mL)

Procedure:

1. Place hot plate in the fume hood to prevent inhalation of fumes when ink cures.
2. Preheat the hot plate to 125°C.
3. Cut the Jacquard silk sheets into four equal rectangles per sheet. The resultant silk cut outs should be 4.25" by 5.5".
4. Cut out the amount sheets desired. Each print creates nine Ag/AgCl-Zn cells – Each Jacquard silk sheet will print 36 cells.
5. Measure and mark the screen base to assist in aligning the silk sheets beneath the patterned screen. Once the desired alignment location is determined, mark the corners of the silk sheet for following prints. The screen will not be transparent to align the design once ink is dispersed on the screen.
6. Collect and place the following supplies into the fume hood on a paper towel:
    a. Screen assembly
    b. Fisher Scientific BD 1 mL Slip Tip syringe

86

        c.   Silver/Silver Chloride ink

        d.   In-house zinc ink

        e.   Ink thinner

        f.   Glass beaker (250 mL) filled with water

7. Shake the silver/silver chloride ink to suspend the silver particles.

8. Place a solvent resistant trash bag in the fume hood to collect waste during printing. See MSDS and technical data sheets for ink and thinner for proper disposal. In summary, liquid waste from either the ink or solvent can be disposed in the solvent waste container. If the ink is allowed to solidify, it can be disposed of in the solid waste container.

9. Align a cut-out sheet of printable silk to the guidelines previously drawn.

10. Tape the side edges of the silk to the screen base using masking tape.

11. Draw 0.3 mL of Ag/AgCl ink into the slip tip syringe.

12. Deposit the ink along the top side of the patterned design of the screen.

13. Using the edge of the squeegee, draw the squeegee through the ink deposited on the screen and across the entire pattern using uniform pressure and constant speed. Repeat this pass twice more.

14. Scrape the excess ink on the squeegee back into the Ag/AgCl ink container.

15. Once again, deposit 0.3 mL of Ag/AgCl ink along the top side of the design and repeat the squeegee passes as before. Two depositions of the ink on the screen with three squeegee passes should uniformly print the design. Lift the screen to ensure this and adjust the number of passes with and without depositing ink accordingly.

16. Lift the screen and remove the masking tape from the silk.

17. Place the silk with the Ag/AgCl print onto the hot plate and let cure for 10-12 minutes (Figure 32)
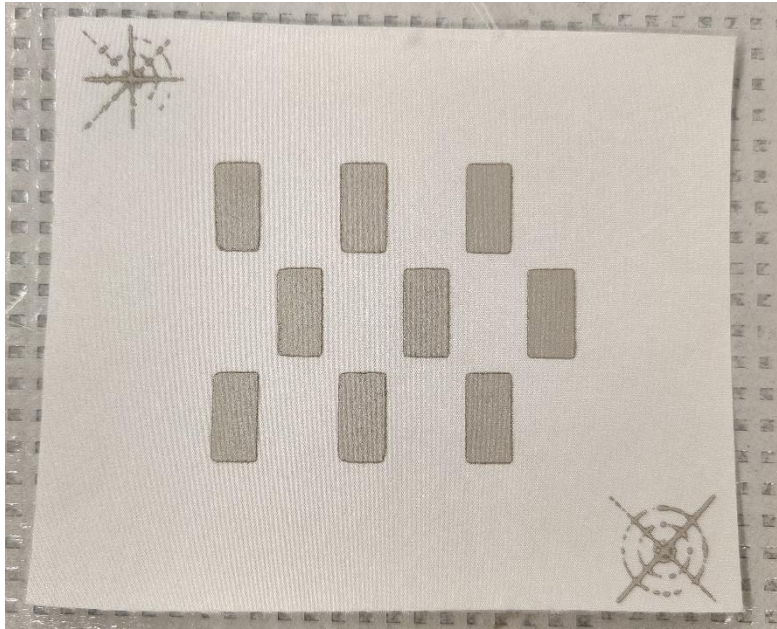

Figure 32. The cured Ag/AgCl print with cell blocks and registration marks.

18. Repeat steps 9-17 until desired number of cells are printed.
19. Using clean room paper towels and 102-03 thinner, clean all the Ag/AgCl ink from the screen and squeegee.
20. Place the Ag/AgCl ink back into the refrigerator.

21. Take a cured Ag/AgCl print and place it underneath the appropriate design for the zinc print. Align the registration marks and tape the silk sheet with masking tape (Figure 33).
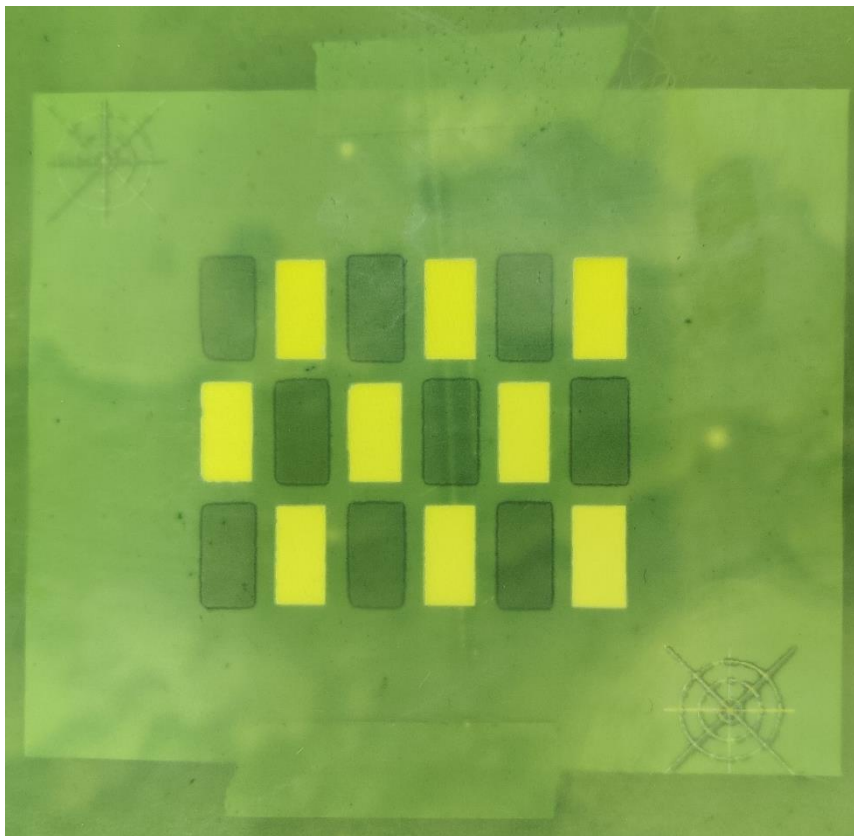

Figure 33. The cured Ag/AgCl print aligned underneath the zinc pattern by aligning registration marks.

22. Draw 0.3 mL of zinc ink into a 1 mL slip tip syringe and deposit it above the screen design. Pass the squeegee across the design as described for the silver/silver chloride ink.
23. Lift the screen and remove the tape from the silk sheet.
24. Place the silk sheet with the printed zinc onto the hot plate and let cure for 10 minutes.
25. Repeat steps 21-24 until all desired cells are printed.

26. Using clean room paper towels, clean the screen and squeegee with deionized water.